


Cite this: *Energy Adv.*, 2024,  
3, 689

# A comprehensive review of entropy engineered GeTe: an antidote to phase transformation

Ranita Basu \*<sup>ab</sup> and Ajay Singh<sup>ab</sup>

Driven by the burgeoning demand for high performance eco-friendly thermoelectric materials in the mid-temperature range (573–773 K), we herein focus on GeTe based alloys that exhibit a high thermoelectric figure-of-merit >2.0 owing to their promising band structure with a conversion efficiency of ~13.3% for the segmented module and ~14% for the single leg device. However, the drawback is the phase transition at ~700 K, which is inevitable, and the irony is that practical application of thermoelectrics has no space for phase transition, as it can be detrimental owing to the unexpected change resulting in deterioration of the devices under operation, thus limiting their mass-market applications either as power generators or as refrigerators. Nevertheless, a comprehensive review is needed for finding ways to cease or abase the phase transformation in the operating temperature regime. In this regard, the most recently developed GeTe-based thermoelectric materials are reviewed coupled with the blooming paradigm, *i.e.*, entropy engineering. The review article thus summarizes the concept of entropy engineering owing to its contribution to boosting thermoelectric performance by increasing the configurational entropy of the system and cites several case studies. Towards the end, future scope and directions were proposed to use entropy tailored GeTe based alloys for the development of high efficiency power generators.

Received 29th January 2024,  
Accepted 20th February 2024

DOI: 10.1039/d4ya00057a

rsc.li/energy-advances

## 1. Introduction

Power generation using the concept of thermoelectricity has proven its reliability in planetary explorations owing to its ability to directly transform heat into electricity. Nonetheless, the doomed efficiency impedes its broad application.<sup>1,2</sup> Innovative research conducted by the thermoelectric community in the last decade has improved the performance of thermoelectric devices significantly, which led to energy harvesting from natural and waste heat and thus provided an alternative solution to mitigate the energy crisis.<sup>3–10</sup> The conversion efficiency of a TE device is defined by the figure of merit ( $ZT$ ) of the thermoelectric alloy given by  $ZT = \frac{\alpha^2 \sigma}{(\kappa_e + \kappa_l)} T$ , where  $\alpha$  implies the Seebeck coefficient,  $\sigma$  implies the electrical conductivity, and  $\kappa_e$  and  $\kappa_l$  are the electronic and lattice thermal conductivities, respectively, at temperature  $T$ .<sup>11,12</sup>

Various strategies were adapted in the past to enhance the  $ZT$ , which include optimization of carrier concentration ( $n$ ) and point defect scattering, causing the peak  $ZT$  to hover around 1. However, the recent concepts and approaches proposed by the

thermoelectric materials researchers, which include the design of new alloys proposed by Slack, *i.e.* phonon glass electron crystals,<sup>13</sup> wherein different properties can be exploited synergistically, have revolutionized the field.<sup>14–18</sup> It is worth mentioning that, in the field of thermoelectricity, it is essentially the inter-coupling of electrons (or holes) and the phonon flow mediated by defects that determines the performance of thermoelectric materials. Thus, defect engineering *via* two fundamental strategies, *i.e.* band engineering and phonon engineering, is frequently considered to tailor thermoelectric properties (as shown in Fig. 1). Using different dopants in the main matrix, the power factor is improved by altering the band structure and simultaneously the lattice thermal conductivity is reduced using microstructure engineering.<sup>15–17</sup> Needless to mention, the oldest and extensively studied thermoelectric alloy, which evoked gusto in the domain of thermoelectrics and led to evolution of new concepts to harvest waste heat energy, is the PbTe system.<sup>19–44</sup> However, Pb toxicity impedes its application, leading to the adoption of eco-friendly modalities. In this regard, the scientific community's attention has now shifted to Pb-free alternatives and one of the analogues is GeTe.<sup>45–50</sup>

However, the challenge with GeTe (as shown in Fig. 2(a)) is that it undergoes phase transformation from the rhombohedral structure ( $\alpha$ -GeTe, space group  $R3m$ ) at ambient temperature to  $\beta$ -GeTe (cubic, space group  $Fm\bar{3}m$ , at 700 K, designated as the

<sup>a</sup> Technical Physics Division, Bhabha Atomic Research Centre, Mumbai-400085, India. E-mail: ranitapaul@gmail.com, ranitab@barc.gov.in; Tel: +91-2225593217

<sup>b</sup> Homi Bhabha National Institute, Training School Complex, Anushaktinagar, Mumbai 400094, India



critical temperature. Intrinsically, GeTe is a degenerate p-type semiconductor with high hole strength. This can be attributed to the fact that during synthesis, plenty of Ge vacancies arise, which cause high carrier concentration, thus conflicting with the generally accepted optimal range.<sup>45–55</sup> To quench the high carrier concentration, group III, IV and V elements are added at the Ge site and Se can be added at the Te site.<sup>49,56–60</sup>

A recent breakthrough in the field of materials science is the preparation of single and multi-phasic high entropy alloys (entropy engineering) with significantly improved mechanical properties. In-depth understanding of the concept of phase engineering accordingly may lead to development of desired crystal structures depending on the applications (Fig. 3(a)). Moreover, to suppress the phase transition, the concept of high entropy or entropy engineering is an emerging paradigm, which focusses on the center of the multicomponent phase diagram instead of the edges in the case of conventional alloys (Fig. 3(b)).<sup>61–68</sup> This perception enables the development of thermoelectric materials with enhanced performance along with long range ordering and simultaneously imposing disorder at short range, which decrease thermal transport and improve electrical transport.

Entropy engineering, thus, embraces introduction of multiple dopants for desired properties to fill the atomic position in the matrix, enhances the configurational entropy and thus subsequently enhances the structural symmetry or overpowers

the structural phase transformation.<sup>69</sup> This causes the increase in the Seebeck coefficient by augmenting the effective mass. In addition, incessant increase of entropy *via* introduction of several elements as dopants intensifies the phonon scattering and thus diminishes the lattice thermal conductivity largely. This high entropy concept has been efficaciously executed in some of the thermoelectric materials, *viz.* Ag<sub>9</sub>GaSe<sub>6</sub>,<sup>72–74</sup> (Cu<sub>7</sub>PSe<sub>6</sub>)<sup>72,74,75</sup> and Cu<sub>2</sub>S with inferior symmetry.<sup>72,73,76</sup>

Hu *et al.* in one of his articles explicitly explained the entropy engineering in SnTe and illustrated how the high entropy effect differs from multi-elemental doping.<sup>71</sup> He explained that high entropy alloying is a subset of multi-principal element alloying and is associated with four core effects (Fig. 4(a)–(c)). In view of this fact, the paradigm can be effective for achieving high thermoelectric performance although with a compromise in the carrier mobility (Fig. 4(d)).

GeTe, being one of the low symmetry thermoelectric materials in the low temperature regime ( $\leq 700$  K), was re-envisioned as a matrix where the hypothesis of high entropy can be realized in order to suppress the phase transition followed by optimization of carrier strength and reduction of thermal conductivity as the performance of pristine GeTe is at the mercy of the high hole concentration and high thermal conductivity.<sup>45–55,77</sup> As illustrated in Fig. 5, GeTe, which remained unexplored for a prolonged period owing to its phase transition in the operating temperature regime and limited



**Ranita Basu**

*Dr Ranita Basu is a Research Scientist in the Physics Group of Bhabha Atomic Research Centre (BARC) and an Assistant Professor in Homi Bhabha National Institute, Mumbai. She joined the prestigious BARC Training School after the completion of her MSc in Chemistry in 2007 at the University of Calcutta. She received her PhD degree in Chemical Sciences in 2015 from Homi Bhabha National Institute,*

*Mumbai for her research topic on “Studies on thermoelectric properties of heavily doped semiconducting alloys for the development of power generators”. Her current research interest includes materials for energy harvesting especially thermoelectric materials for tapping waste heat energy, which include chalcogenides such as bismuth-telluride, lead telluride, tin telluride, silicon-germanium alloys, etc. Her research interest also includes fabrication of power generators with enhanced efficiency using new contact materials. She has published more than 50 peer reviewed journal papers with review articles on thermoelectric materials and device fabrication in high impact journals. She is a recipient of Emerging Women in Material Science Award sponsored by Wiley.*



**Ajay Singh**

*Dr Ajay Singh is presently working as Scientific Officer (H) at the Technical Physics Division of Bhabha Atomic Research Centre (BARC) Mumbai. He joined BARC in 1999 after graduating from the 42nd Batch of Training School. He completed his MSc (Physics) at HNB Garhwal University in 1997 and PhD at Mumbai University in 2004. He is a recipient of the Humboldt Post-doctoral fellowship (2005–2007), the DAE Young*

*Scientist Award for excellence in the Science and Technology – 2007, the National Academy of Sciences India (NASI) Young Scientist Platinum Jubilee Award – 2010, the DAE Solid State Physics Symposium Young Achiever Award (DAE SSPS YAA) – 2010, the Indian National Science Academy (INSA) Young Scientist Medal – 2012, the DAE Science & Technical Excellence Award – 2015 and the MRSI Medal – 2022. He is a fellow of the Maharashtra Academy of Sciences. His present research interests include design and development of high performance thermoelectric materials, thermoelectric power generators and essential interfacial electronics required for applications of thermoelectric generators. He has published 150 peer reviewed journal papers and has been granted 1 US patent.*



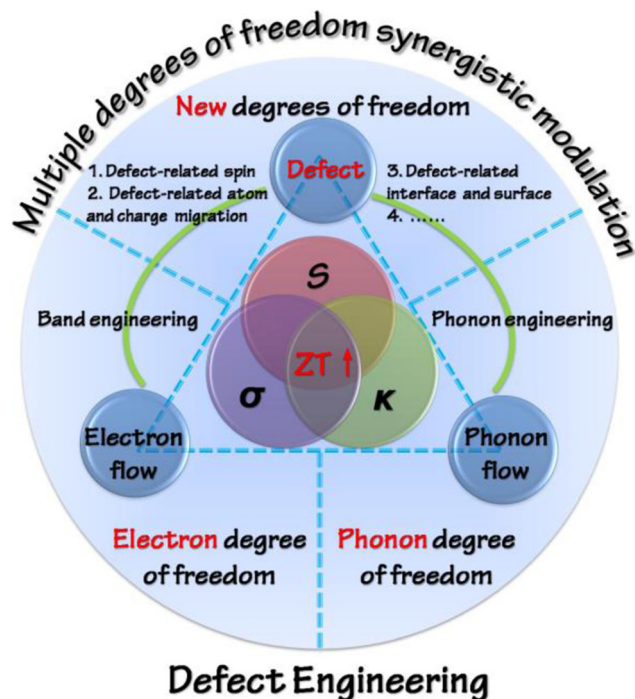


Fig. 1 Schematic representation displaying the strategies meant for optimization of  $ZT$  on the basis of defect engineering with the perception of synergistically modulating multiple degrees of freedom. Reproduced with permission from Copyright © 2016, American Chemical Society.<sup>18</sup>



Fig. 2 Characteristics of the GeTe alloy as a thermoelectric material. Crystal structures of (a) rhombohedral GeTe and (b) cubic GeTe along with the respective primitive cells of (c) rhombohedral GeTe and (d) cubic-GeTe. Reproduced with permission from © 2019 Wiley-VCH Verlag GmbH & Co. KGaA, Weinheim.<sup>51</sup>

knowledge on the tailoring of electronic band structure, has regained attention. This is attributed to the better understanding of the electronic band structure *via* density functional theory and validation with the experimental findings.<sup>47,77</sup>

Initially, chemical doping with single elements (such as In, Pb, Bi and Sb) was accomplished to optimize the carrier concentration,<sup>78,79</sup> but the results showed that dual doping is preferred to obtain  $ZT$ s exceeding 2.0,<sup>79–83</sup> such as for  $\text{Ge}_{1-x-y}\text{Sb}_x\text{Zn}_y\text{Te}$ ,<sup>84</sup>  $\text{Ge}_{1-x-y}\text{Sb}_x\text{In}_y\text{Te}$ ,<sup>54</sup> and  $\text{Ge}_{1-x-y}\text{Bi}_x\text{Cd}_y\text{Te}$ .<sup>85,86</sup> As illustrated in Fig. 6, the vast list of elements in the periodic table has promoted the progress of GeTe thermoelectrics. The highlighted elements in the periodic table, *viz.* Ti, V and Cr, were doped to boost the  $ZT$  of GeTe by reducing the charge carrier scattering or refining the band structure and thus aiding in enhancing electron transport properties. La and Nd were also beneficial for tailoring the band structure; aliovalent dopants such as Bi and Sb or other elements of group 15 were utilized to optimize the charge carriers along with halogens (I); Sn introduces Rashba splitting; and In introduces resonant levels. Doping at the anionic site is advantageous to introduce point defect scattering of phonons and thus reduces the lattice thermal conductivity. However, the problem is that phase transition still persists, which is detrimental to thermoelectric devices,<sup>87</sup> as it leads to stress due to mismatch in the thermal expansion coefficient in different phases, with the concentration of charge carriers (holes for GeTe) deviating from the optimized value. Evidently, one of the key issues with GeTe based alloys is to reduce the phase transition towards the lower temperature so that the applications of high symmetrical structures can be extended over a wide temperature regime. Although considerable headway has been made with the high entropy materials towards designing novel alloys for thermoelectric applications, in this review our aim is to solve the fundamental problem pertaining to phase transition in GeTe and suppressing it to ambient temperature from 700 K *via* entropy engineering so that the alloys with superior band structures can be utilized for the fabrication of thermoelectric devices.<sup>87–93</sup>

## 2. Genesis of entropy engineering

The term “entropy” was defined and developed in 1870 by the famous scientist Ludwig Boltzmann by probing the statistical behavior of the microscopic constituents of a system.<sup>94,95</sup> The hypothesis proposed by Boltzmann states that there lies a correlation between the entropy or randomness of a system in a predefined state and the possibility of the presence of a given state:

$$S = k_B \ln \omega, \quad (1)$$

where  $S$  defines the contribution of disorder or entropy of the system for the predefined state,  $k_B$  is the Boltzmann constant and is given by  $1.38 \times 10^{-23} \text{ J K}^{-1}$ , and  $\omega$  is the probability of distribution of the constituents in the system.

For an alloy system, the Gibbs energy of mixing is given by:

$$\Delta G_{\text{mix}} = \Delta H_{\text{mix}} - T\Delta S_{\text{mix}}, \quad (2)$$

where  $\Delta G_{\text{mix}}$ ,  $\Delta H_{\text{mix}}$  and  $\Delta S_{\text{mix}}$  are the free energy, enthalpy and entropy of mixing respectively. Eqn (2) shows that at constant  $\Delta H_{\text{mix}}$  enhanced entropy of mixing will lead to lowering of





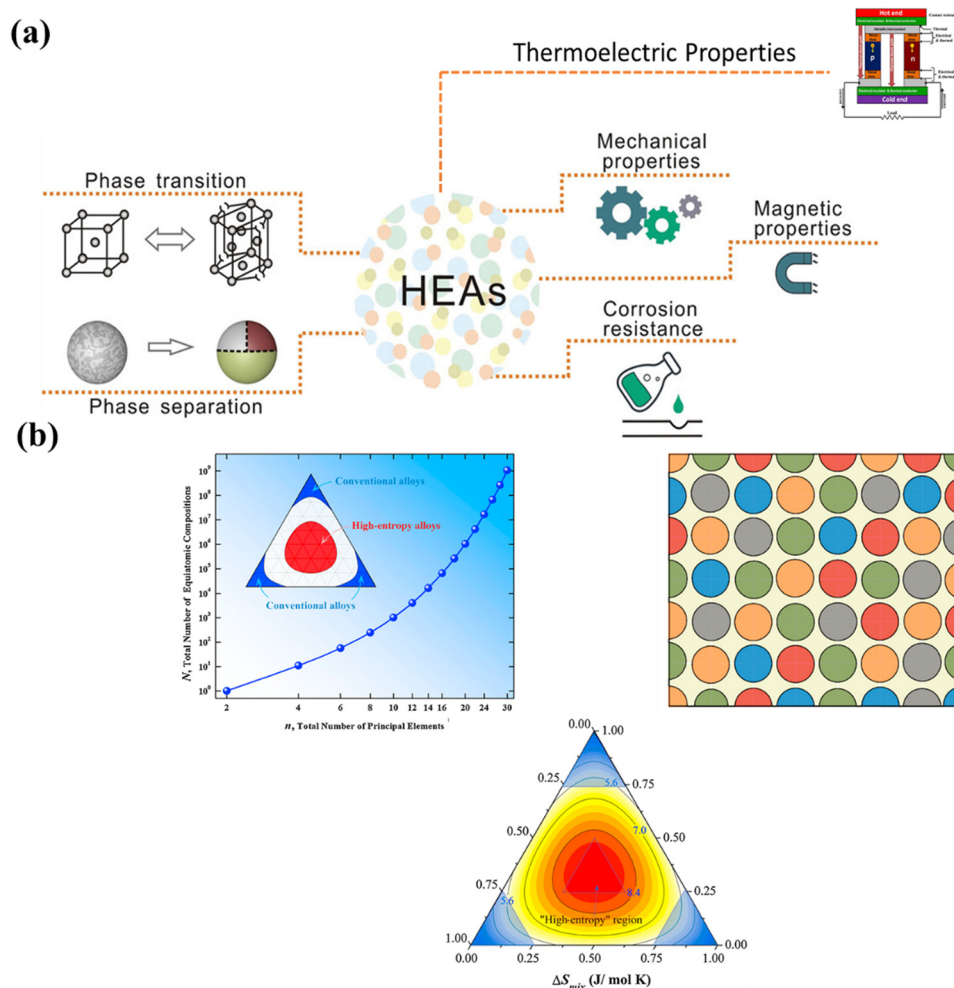


Fig. 3 (a) Schematic illustration depicting phase engineering in high entropy alloys, which governs their mechanical properties and accordingly decides their applications and (b) demonstration of the change in the equiatomic compositions as the principal element varies. The diagram also depicts how the phase space enhances for the high entropy alloys in comparison to the conventional alloys. Reproduced and adapted from ref. 69 and 70. Copyright © 2020 Wiley-VCH Verlag GmbH & Co. KGaA, Weinheim, Copyright © 2016 Elsevier Ltd, respectively, and under the terms of the Creative Commons CC-BY-NC-ND license.<sup>62</sup>

$\Delta G_{\text{mix}}$  and thus will result in an alloy system with high stability. Thus, increasing the entropy of mixing has a remarkable impact on the microstructure of the material and subsequently on its macroscopic properties. In this regard, the aim is to maximize the  $\Delta S_{\text{mix}}$ . In thermodynamics, the configurational entropy of mixing for  $n$  components to have random solid solution is given by:

$$\Delta S_{\text{mix}} = -R \sum_{i=1}^n C_i \ln C_i, \quad (3)$$

where  $C_i$  is defined as the molar concentration of the  $i$ th constituent and  $R$  is the universal gas constant. Eqn (3) indicates that  $\Delta S_{\text{mix}}$  of an alloy can be maximized by designing the alloy with an equimolar ratio of multiple principal elements, which can be defined as  $C_i = \frac{1}{n}$  and upon substitution in eqn (3) gives:

$$\Delta S_{\text{mix}} = -R \left( \frac{1}{n} \ln \frac{1}{n} + \frac{1}{n} \ln \frac{1}{n} + \dots + \frac{1}{n} \ln \frac{1}{n} \right) = R \ln n \quad (4)$$

From eqn (4), it can be concluded that for a ternary alloy system,  $\Delta S_{\text{conf}}$  is  $1.10R$  and accordingly it increases with the increase in the

number of elements in the alloy system. Unlike the philosophy of traditional alloy design, the entropy maximization concept emphasizes the entropic contribution instead of the contribution of the cohesive energy to the free energy. This influences the thermodynamic stability of the alloy system at finite temperature and favours the solid-solution formation with high symmetrical crystal structure. The thermoelectric researchers worldwide are now inclined towards the novel philosophy of entropy engineering by adding multiple elements for designing advanced alloys with symmetric crystal structures to boost the Seebeck coefficient and decrease the phonon conduction simultaneously. This enhances the thermoelectric performance unlike the earlier trend of designing complex crystal structures for reducing the lattice thermal conductivity alone.<sup>87–93</sup>

### 3. GeTe as a thermoelectric material

The entire essence of thermoelectricity is having a high  $ZT$  thermoelectric material for the fabrication of efficient devices.<sup>9,62</sup> This involves development either of high temperature power generators or near room temperature





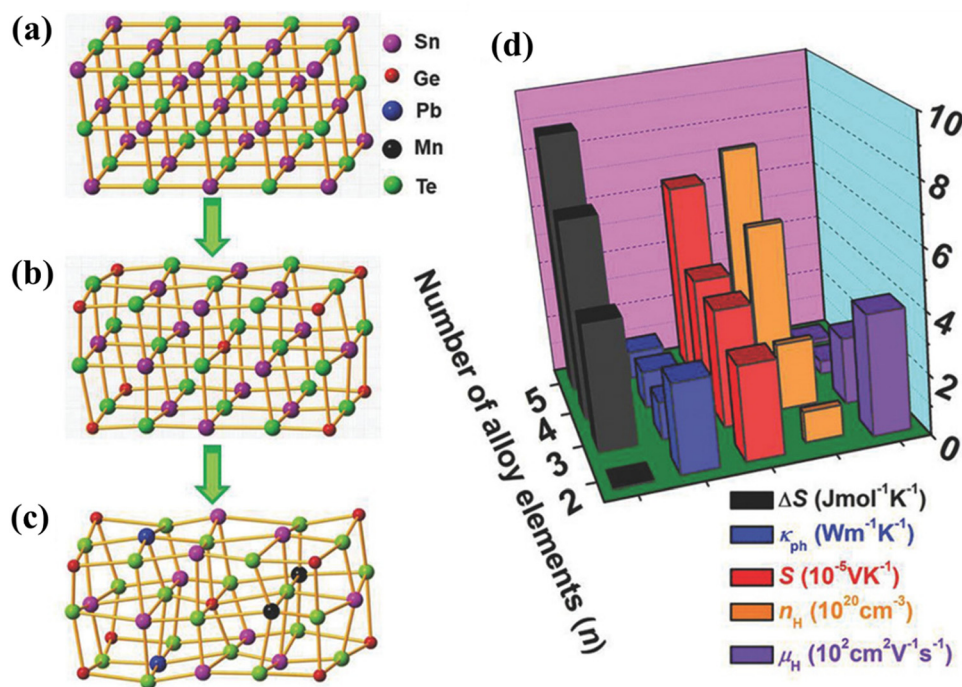


Fig. 4 (a)–(c) Schematic illustration depicting the change in lattice distortion with the increase in the addition of dopants in symmetric IV–VI chalcogenides. (d) Representation to demonstrate the nature of change in properties: (i) entropy of mixing  $\Delta S$ ; (ii) lattice thermal conductivity  $\kappa_{\text{ph}}$ ; (iii) Seebeck coefficient  $S$ ; (iv) carrier concentration  $n_{\text{H}}$ ; and (v) carrier mobility  $\mu_{\text{H}}$  at 300 K for highly symmetric IV–VI chalcogenides. Reproduced with permission from ref. 71. Copyright © 2018 Wiley-VCH Verlag GmbH & Co. KGaA, Weinheim.

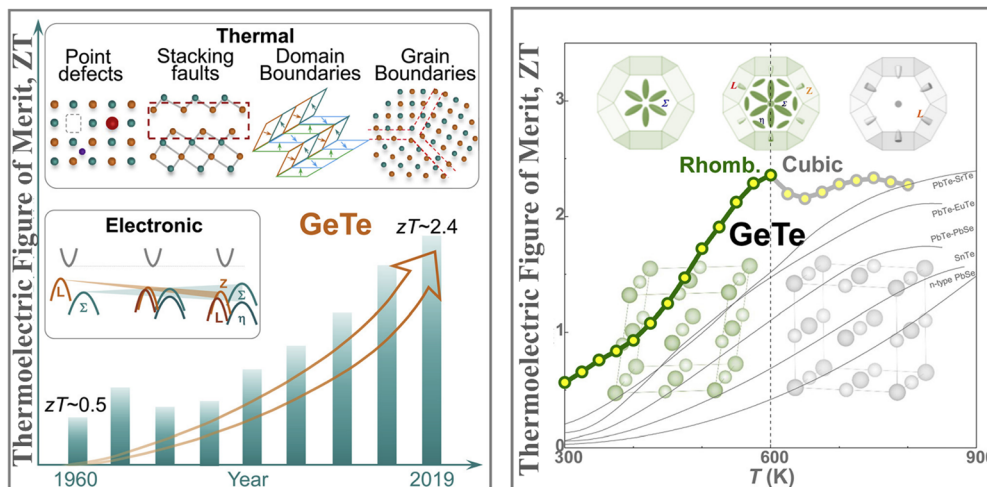
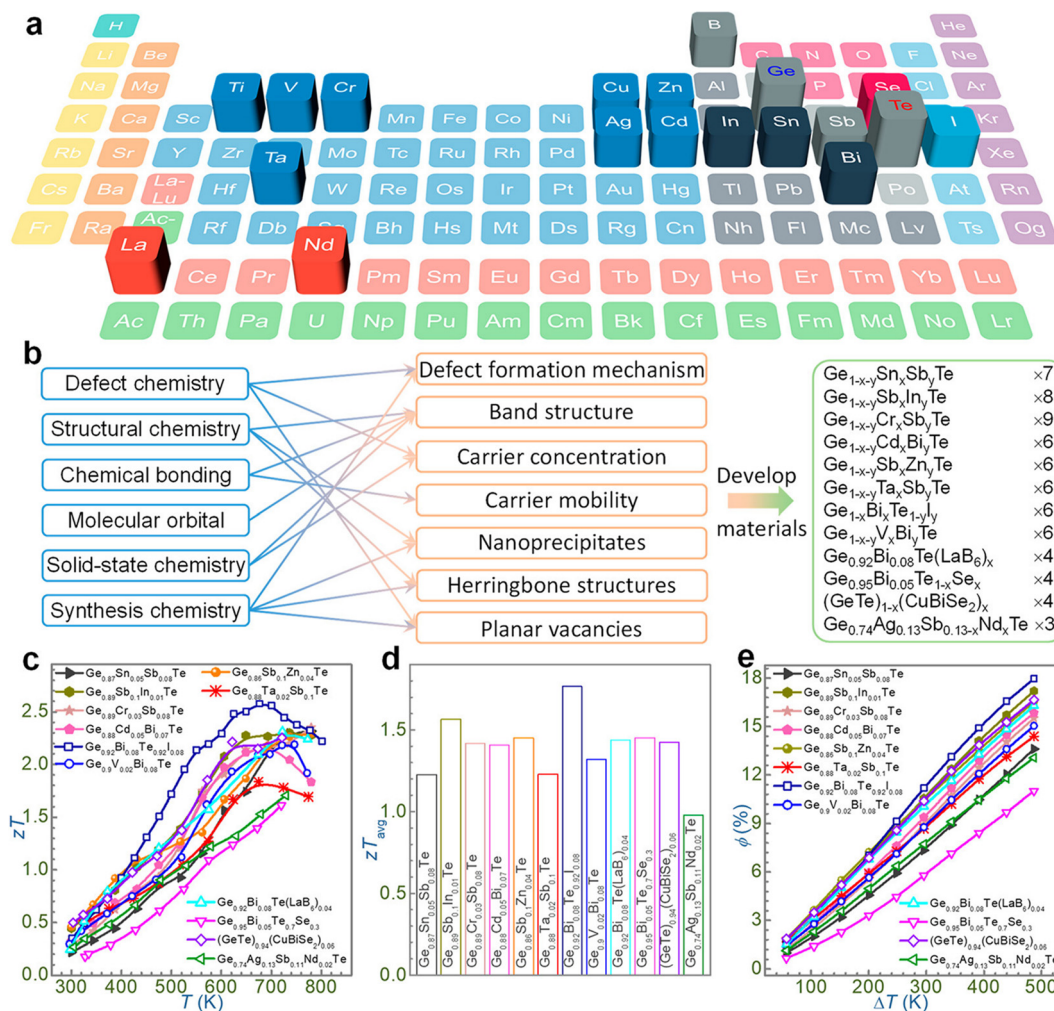


Fig. 5 Schematic representation demonstrating electronic and thermal contribution to the high thermoelectric performance of GeTe over the years. Detailed investigation revealed that slight symmetry reduction is beneficial over high symmetry GeTe based alloys for thermoelectric applications. Reproduced and adapted from ref. 47 and 77 under the terms of the Creative Commons CC-BY-NC-ND license.

refrigerators. The widely used materials for this niche application include silicides,<sup>96–98</sup> chalcogenides,<sup>19–44,99–101</sup> half-Heusler,<sup>102,103</sup> Zintl,<sup>104,105</sup> etc. Among chalcogenides, Pb–X, Ge–X, and Sn–X, where X = S, Se and Te, are widely used for power generators in the mid-temperature regime *i.e.*  $500\text{ K} \leq T \leq 800\text{ K}$ ,<sup>106,107</sup> whereas  $\text{Bi}_2\text{Te}_3$ <sup>108–110</sup> and  $\text{Ag}_2\text{Se}$ <sup>111–116</sup> are for near room temperature applications.

In mid-temperature applications, IV–VI chalcogenides are well-known thermoelectrics owing to their remarkable band structures<sup>19–55</sup> and pioneering bonding technique, which is termed as “metavalent bonding”.<sup>117–122</sup> Among them PbTe based alloys stand out. This is because PbTe based alloys possess optimized carrier concentration and so the proven strategies, which guarantee high  $zT$ , can be realized efficiently.



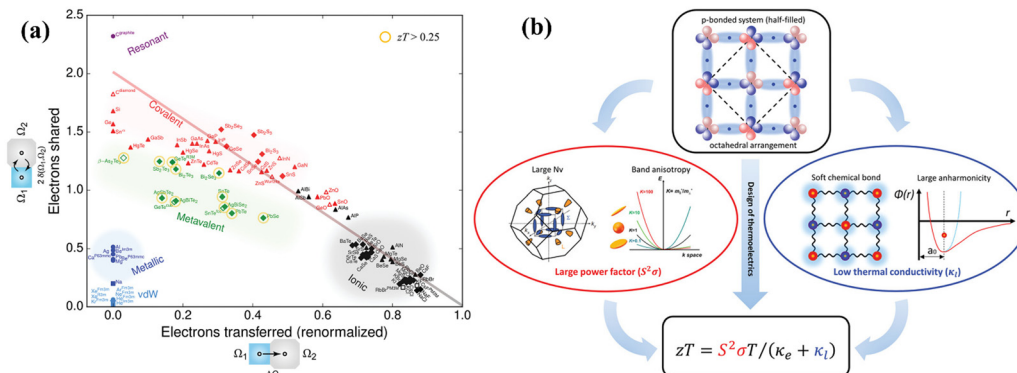
**Fig. 6** Outline of the recent outcomes of GeTe thermoelectrics in terms of chemical principles. (a) Elements in the periodic table (highlighted) employed to tailor the GeTe thermoelectrics; (b) strategies utilized to enhance the thermoelectric performance on the basis of chemical disciplines and the GeTe derivatives developed so far; (c)–(e) summary of the results on GeTe thermoelectrics obtained by different groups. Reproduced and adapted from ref. 79, Copyright © 2022, American Chemical Society.

Fig. 7(a) demonstrates the bonding mechanism involved in various compounds. The  $x$ -axis depicts the electrons transferred, which is more prominent in the case of ionic compounds and the  $y$ -axis demonstrates the electrons shared, which is more pronounced in covalent compounds. An emerging bonding technique known as metavalent bonding is mapped in the plot. These alloys with metavalent bonding show exceptional thermoelectric performance (illustrated in Fig. 7(b)) owing to their electronic band structure with high band degeneracy and significant band anisotropy to empower the coupled power factor. The bonding mechanism also illustrates soft chemical bonds along with high anharmonicity, which subdues the lattice thermal conductivity. The bonding mechanism thus interweaves the outstanding thermoelectric performance of octahedrally coordinated chalcogenides. To avoid Pb-toxicity, the hunt for alternatives<sup>123–126</sup> has led to the detailed investigation of GeTe based alloys from the thermoelectric point of view, as they have been known since the

1960s. They remained unexplored due to phase transition at  $\sim 700$  K as discussed earlier.<sup>127–129</sup>

The slight distortion of high symmetric cubic rock-salt structure along the [111] direction with an interaxial angle of  $\alpha = 88.2^\circ$  at 300 K is approximated as rhombohedral GeTe with three longer and three shorter bonds in octahedral geometry.<sup>127–129</sup> However, with increase in temperature, known as the critical temperature,  $\sim 700$  K, which may change depending on the carrier concentration to  $(650 \pm 100 \text{ K})$ <sup>128</sup> as illustrated in Fig. 8(a), the rhombohedral transits to cubic lattice displaying symmetrical variation to its average. This structural transition is suspended and the cubic rock-salt structure stabilizes prominently as the cation–anion pair changes to a heavier cation *i.e.*  $\text{Ge} \rightarrow \text{Sn} \rightarrow \text{Pb}$ . This is attributed to the differences in hybridization of orbitals and bonding ionicity. For GeTe, the structural deformation to low symmetric rhombohedral from the symmetrical cubic phase is predominantly due to the stereochemical activity of the lone pair electrons on the





**Fig. 7** (a) A 2-dimensional map to showcase the electron transfer and bonding in materials. *x*-Axis denotes the number of relative electrons transferred and *y*-axis denotes the sharing of electrons among neighboring basins via the quantum topological method. Octahedrally coordinated chalcogenides with unusual properties (high values of  $\epsilon_{\infty}$ , large anharmonicities, an intermediate electrical conductivity, pronounced electron–phonon coupling, and an effective coordination number mismatch with ordinary covalent bonding) are depicted in green and have been termed as metavalent bonding compounds. Reproduced and reprinted from ref. 117, © 2019 RWTH Aachen University. Published by Wiley-VCH Verlag GmbH & Co. KGaA, Weinheim. (b) Schematic representation depicting the exceptional thermoelectric performance of octahedral chalcogenides having metavalent bonding. Reproduced and reprinted from ref. 119, © 2019 The Authors. Published by Wiley-VCH Verlag GmbH & Co. KGaA, Weinheim.

*s*-orbital of Ge and is related to the intense hybridization between the *s*-orbital of the cation and the *p*-orbital of the anion. This provokes a remarkable deformation in the allocation of electrons, which in due course causes the decline in the

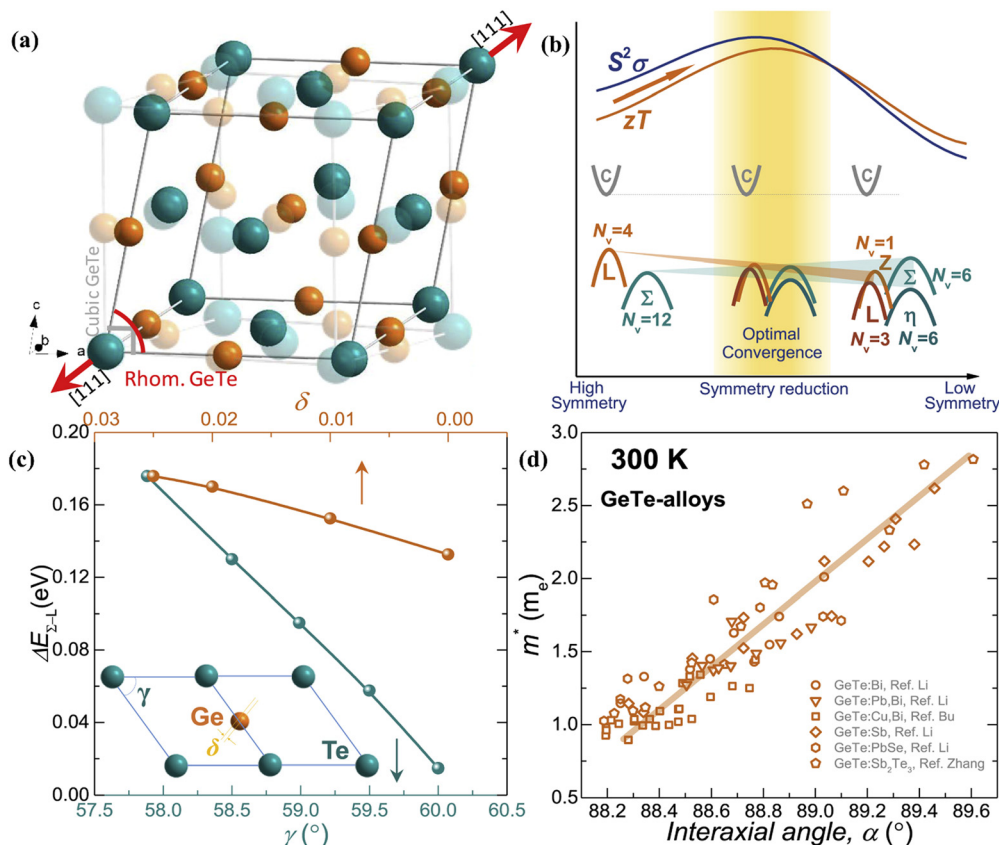


**Fig. 8** Schematic details of the electronic basis of GeTe: (a) crystal structures depicting both rhombohedral (coloured) and cubic (transparent) phases of GeTe; (b) schematic representation illustrating that slight symmetry breaking is beneficial for enhanced band convergence leading to high band degeneracy; and (c) depiction demonstrating the change in the energy offset, *i.e.*, the difference in the L- and  $\Sigma$  valence bands with the variation in the rhombohedral angle ( $\gamma$  in the primitive cell) and displacement from the off-center ( $\delta$ ) (the inset displays the primitive cell,  $\gamma < 60^\circ$  and  $\gamma = 60^\circ$  for *r*-GeTe and *c*-GeTe respectively); (d) change in the density-of-state effective mass ( $m^*$ ) with the variation in the rhombohedral angle ( $\alpha$ ) at 300 K. for GeTe-alloys. Reproduced and adapted from ref. 47 under the terms of the Creative Commons CC-BY-NC-ND license.





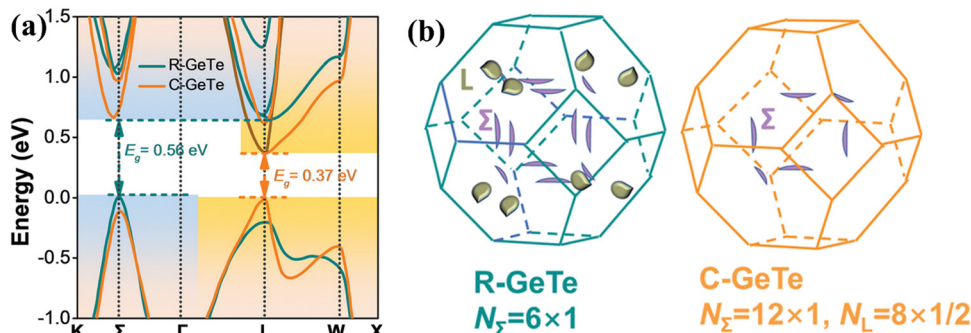


Fig. 9 (a) Calculated electronic band structure of GeTe featuring both R-GeTe (rhomboidal GeTe) and C-GeTe (cubic GeTe) respectively; (b) calculated Fermi surfaces for both R-GeTe and C-GeTe considering spin-orbit coupling. Reproduced and reprinted from ref. 45, © 2020 Wiley-VCH Verlag GmbH & Co. KGaA, Weinheim.

structural symmetry. From the viewpoint of transport of charge, an enhancement of either s-p hybridization or ionicity of the bond augments the isotropic nature of the light valence band (L-band), which eventually decreases its  $\frac{m^*}{m_1^*}$  and thus makes it superior among group IV-VI chalcogenides.<sup>129-135</sup> Fig. 8(b) demonstrates that although the cubic structure (at elevated temperature) has high symmetry in comparison to the rhombohedral structure at low temperature, as far as thermoelectricity is concerned, slight symmetry breaking is preferred as it leads to high band degeneracy. In addition, the doping at the cationic site displaces Ge from the off-center and therefore the energy difference between the light (L) and heavy ( $\Sigma$ ) valence bands reduces and subsequently aids in valence band convergence (illustrated in Fig. 8(c)). The doping at the cationic site (Fig. 8(d)) also increases the interaxial angle, the density-of-state effective mass and consequently the Seebeck coefficient.

### 3.1. Electronic properties of GeTe

The band diagram of cubic-GeTe is analogous to those of PbTe and SnTe, where the maxima of the valence band and minima of the conduction band lie at the L-point of the Brillouin zone ( $N_v = 4$ ) and thus lead to the direct band gap. However, the secondary valence band, which is located in the  $\Sigma$  direction, is energetically lower than the L band with a high band degeneracy of  $N_v = 12$  and an energy offset  $\Delta E_{L-\Sigma} \sim 64$  meV, as depicted in Fig. 9.<sup>45,47</sup> The low energy offset value indicates that the two valence bands are strategically placed for convergence at elevated temperature in comparison to PbTe ( $\Delta E_{L-\Sigma} \sim 100$  meV)<sup>31</sup> and SnTe ( $\Delta E_{L-\Sigma} \sim 300$  meV).<sup>15</sup> This implies a favorable pathway for transportation of charge carriers and is self-explanatory for realization of enhanced  $ZT$  in the symmetric GeTe phase at elevated temperature.

Nevertheless, the location of the L and  $\Sigma$  bands at different Brillouin zones shows different responses when lattice distortion occurs along the [111] direction, *i.e.* the L-point of the Brillouin zone. Thus, directional lattice distortion was explicitly employed to manipulate the energy of the bands. This causes a substantial decrease of L-band energy and thus the maximum of the valence band is the  $\Sigma$  band in the rhombohedral GeTe.

Moreover, the reduction in symmetry or symmetry breaking in the crystal structure separates the L-band with 4 carrier pockets into 3 L and 1 Z. Simultaneously, the 12 carrier pockets in the  $\Sigma$  band splits into 6  $\Sigma$  and 6  $\eta$  (illustrated in Fig. 8(b)).<sup>45,47,77,136</sup> This creates a hindrance in the rhombohedral phase to attain optimum band convergence and thus makes it an inferior candidate as a thermoelectric material in comparison to the usual cubic analogue.<sup>136</sup> However, the increased degree of freedom augments the tuning of band energies and is adequate to converge all the bands. This mode of crystal structure engineering, which facilitates the band structure manipulation, opens an avenue such that slight symmetry deviation is electronically favorable towards enhanced thermoelectric performance.<sup>77,136</sup>

### 3.2. Entropy stabilized GeTe

The noteworthy feature of the high entropy concept in thermoelectrics is ultralow lattice thermal conductivity. This is because of the fact that the extremely distorted lattices obtained in high-

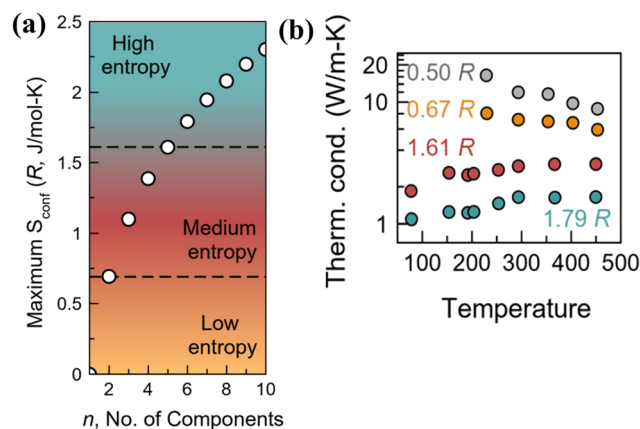


Fig. 10 (a) Schematic representing the variation in categories in configurational entropy with the increase in the number of components; the plot shows that high entropy can be attained when the number of constituent elements is at least 5, which share a similar crystallographic site. (b) Plot demonstrating the lowering of thermal conductivity with the increase in the configurational entropy. Reproduced and adapted from ref. 137. Copyright © 2023, American Chemical Society.



entropy alloys induce high strain, which eventually causes effective phonon scattering and minimizes the lattice thermal conductivity to an extent that it resembles the unique phonon glass performance. Nonetheless, the ideal thermoelectric alloy with enhanced behavior should exhibit “phonon-glass-electron-crystal” behavior.<sup>13</sup> In high-entropy alloys, attaining electron-crystal properties is the bottleneck.<sup>137</sup>

As discussed earlier, the “high-entropy alloy” concept, which eschews the traditional paradigm of “base element” concept, involves designing alloys by shifting the focus from the vertices to the central part of the phase diagram (Fig. 2(b)). This radical deviation, which involves multiple elements (contradicting the rule of Parsimony by Pauling<sup>138</sup>) causing complexity and disorder in the unit cell, enlarges the chemical space. This is due to the reason that addition of multiple elements instigates disorder and complexity in the lattice, amplifies the chemical space and thus unearths the design of new thermoelectric alloys. On a lighter note, it is noteworthy to mention that any material that qualifies for technological applications, although widely known for exquisite purity, essentially needs a finite level of substitutional disorder for its extensive use. The burgeoning demand for high entropy thermoelectric alloys takes advantage of these emerging properties essential for diminishing the lattice thermal conductivity

without compromising the charge transport. Moreover, the increase in the compositional space with the addition of new elements leads to entropy driven structural stabilization, which eventually leads to a highly symmetrical cubic structure possessing a high Seebeck coefficient and band degeneracy and thus enhanced thermoelectric performance.<sup>137,139–141</sup> Fig. 10(a) demonstrates the different levels of entropy and the change in the configurational entropy of the system with the increase in the number of components. As the configurational entropy increases, the thermal conductivity reduces as desired in thermoelectrics (Fig. 10(b)).

However, the topic of high entropy faces linguistic problems and the terminology has evolved continually with time. This is because canonically multiple elements sharing a common crystallographic site are termed as solid solutions. Thus, to distinguish solid solutions from high entropy alloys, a further criterion was essential and this is where unanimous consensus was lacking.<sup>137,139</sup> Thus, to have a model for the expansion of enhanced performance thermoelectric materials, a suitable design of the composition of the materials and temperature of operation is essential. For high-entropy GeTe based alloys, analysis of the properties in different temperature regimes and at different chemical compositions was carried out by Li *et al.* using an interpretable machine learning workflow. The

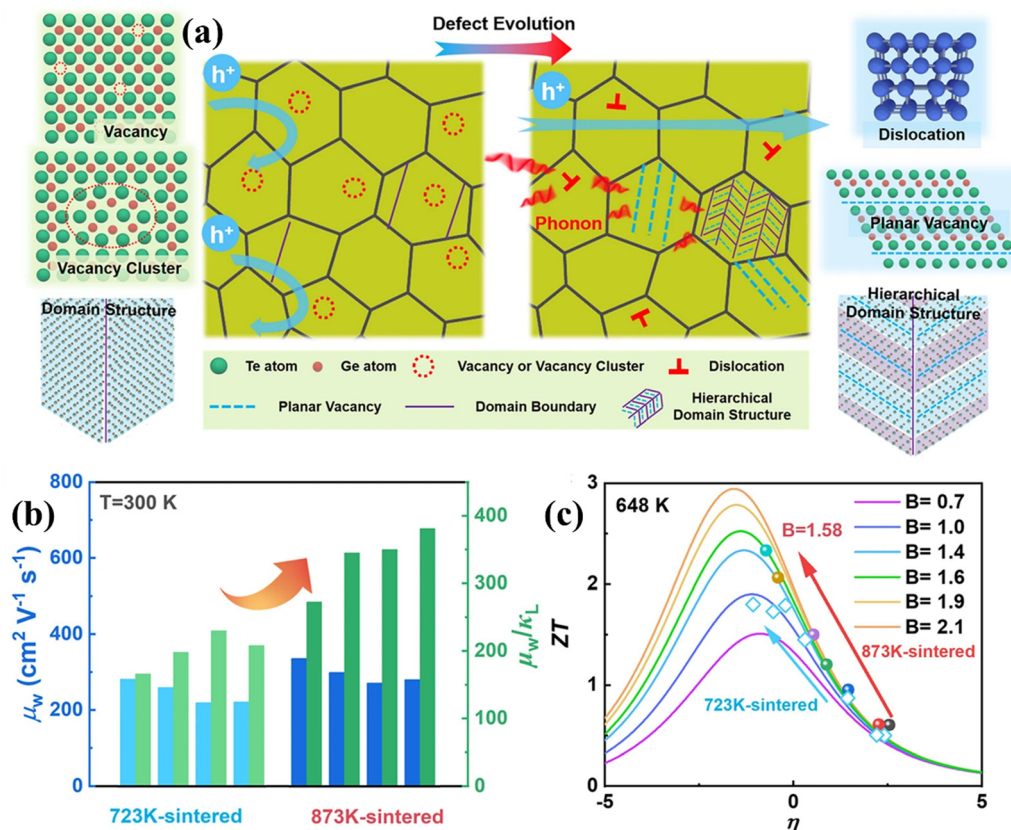


**Fig. 11** (a) Schematic demonstrating the nature of carriers and phonons in the GeTe-derivatives with hierarchical architecturing; (b) plot displaying  $\mu_w$  (weighted mobility) and  $\mu_w/\kappa_L$  for Ge-deficient samples at 300 K (sintered at 873 K), with respect to the samples sintered at 723 K, and (c) ZT value with respect to the reduced Fermi potential having different quality factors at 648 K. Reproduced and adapted from ref. 140 under the terms of the Creative Commons CC-BY-NC-ND license.



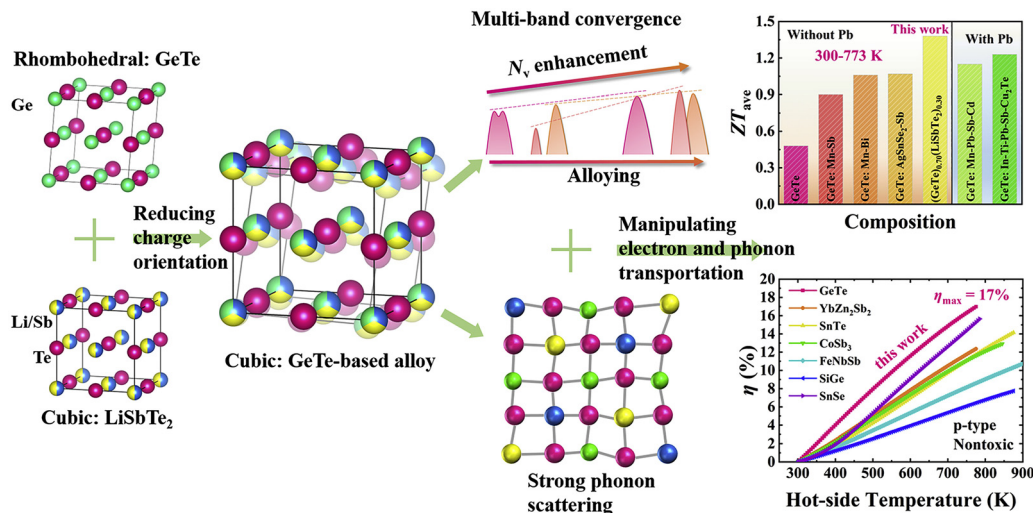


Fig. 12 Schematic demonstration of the origin of crystal structure and the factors responsible for enhanced thermoelectric performance of the GeTe-derivatives. Reproduced and adapted from ref. 142, under the Creative Commons CC-BY-NC-ND license.

methodology involves constructing the dataset from experiments based on preceding research on thermoelectrics and subsequently descriptors are established depending on the atomic features.<sup>131</sup> To choose pertinent features, some of the feature selection mechanisms, *viz.*, Pearson correlation, exhaustive and univariate feature selection, are considered.

The elected features are then utilized in the ZT value, which is a target variable for exercise and testing. Global interpretability, which includes examination of the contribution of the interactive parameters to ZT (target variable), local interpretability approaches, choice of materials and optimization of performances, reveals that the ZT values of the thermoelectric

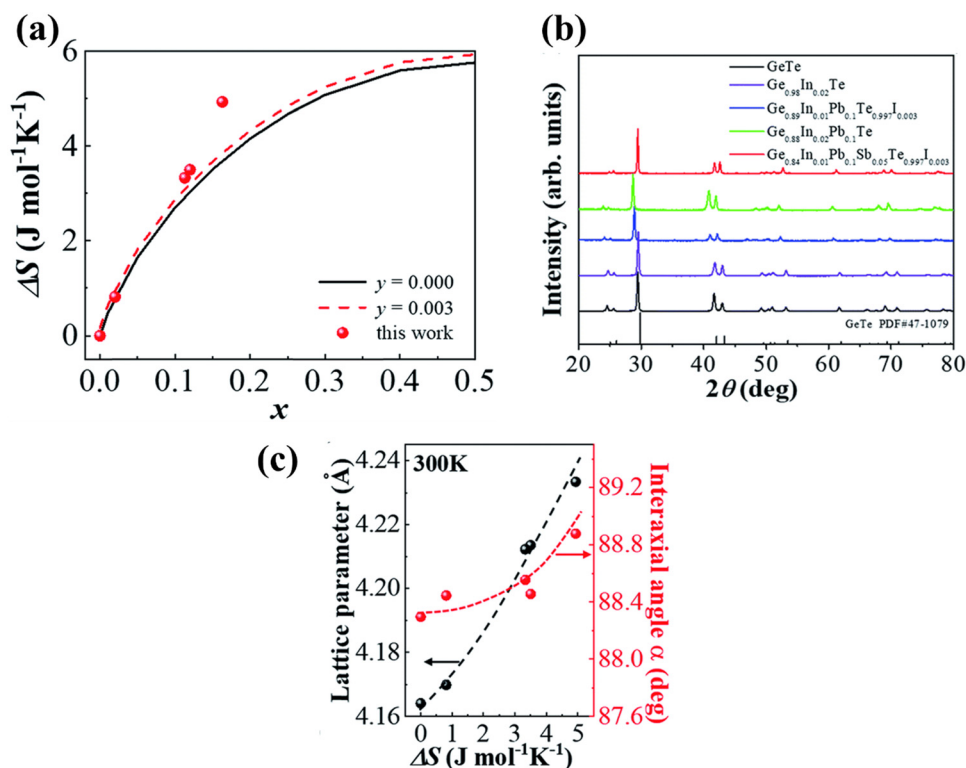


Fig. 13 (a) Plot showing the increase in the configurational entropy with the increase in the constituents of the alloy; (b) powder XRD patterns of GeTe and its derivatives at room temperature. The room temperature GeTe phase resembles the rhombohedral crystal structure and no appreciable secondary phase was seen with the addition of dopant elements; (c) change in the lattice parameters along the direction of  $a$ -axis and so the variation in the interaxial angles with the increase in  $\Delta S$ . Reproduced and reprinted from ref. 144 with permission from the Royal Society of Chemistry.





alloys are primarily controlled by the temperature with little impact of molar volume and electronegativity. By applying interpretable machine learning tools, the prediction and optimization of the performance of the thermoelectric alloys can be assessed for samples with prior knowledge. This enables a thorough approach towards designing workflow apart from assessment and forecast of the thermoelectric properties of alloys. This methodology was used to select and develop high entropy GeTe-based alloys with enhanced performance.

### 3.3. Futuristic GeTe based alloys via entropy engineering

GeTe and its derivatives, being non-toxic among group IV–VI elements, have the proficiency to replace the widely studied PbTe alloys because of their high toxic load. However, due to low symmetry rhombohedral structure, which is responsible for the generation of the ferroelectric domain, abundant microstructures are available to optimize for the enhancement of

thermoelectric performance. Recent advancements in the solid-state physics and the techniques involved in the synthesis provide an efficient means of enhancing the thermoelectric performance.

One of the difficulties associated with GeTe is high carrier concentration ( $\sim 10^{21} \text{ cm}^{-3}$ ) due to the intrinsic Ge vacancies, which has a negative impact on thermoelectricity (depicted in Fig. 11(a)–(c)).<sup>140</sup> Moreover, these intrinsic vacancies restrict the carrier transport and thus deteriorate the mobility of the charge carriers. Here, lies the role of chemical principles for the enhancement of thermoelectric properties. To obtain optimized properties, the dopants are screened, which is generally directed by the chemical valencies and defect chemistry.<sup>79</sup> In addition, dopants are also added to improve the electronic transport properties based on the intense understanding of the molecular orbital theory and to reduce the lattice thermal conductivity by strengthening the phonon scattering with the

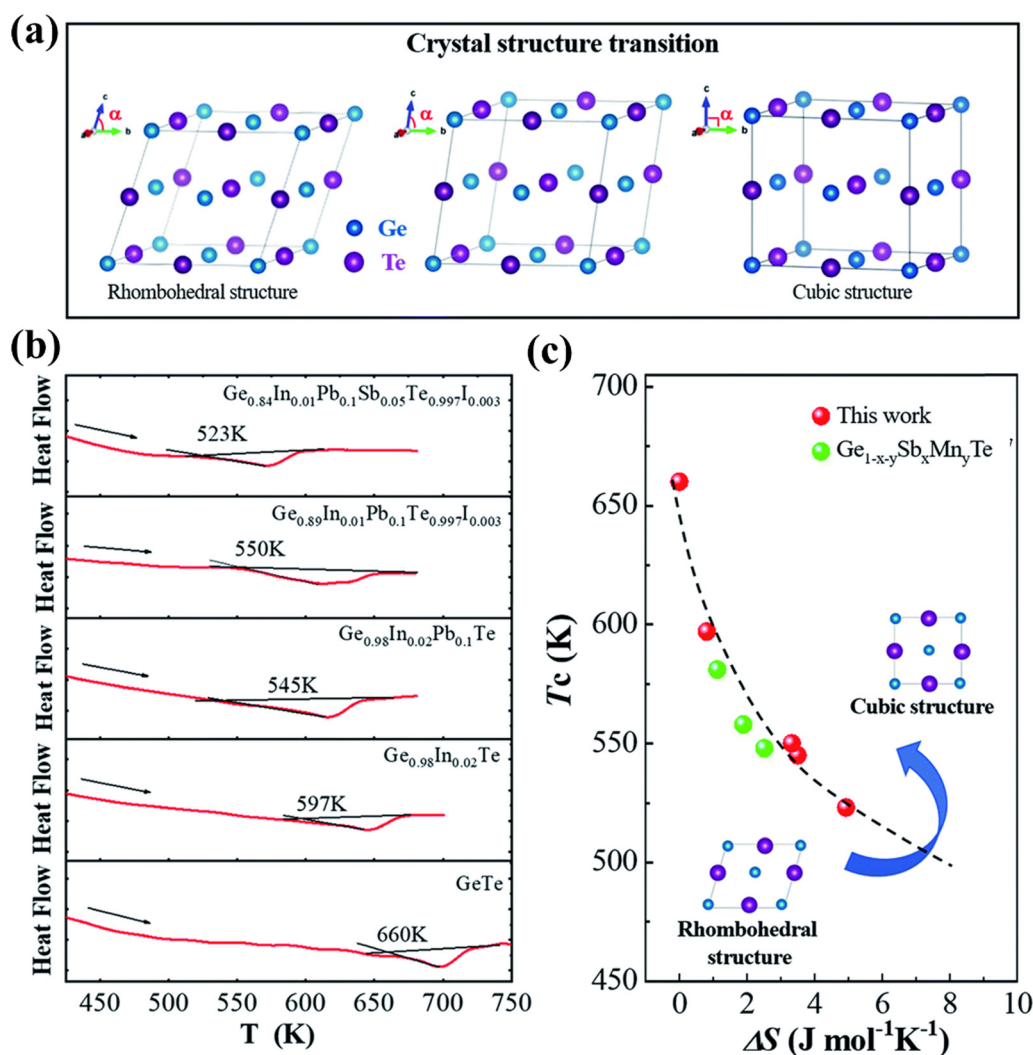


**Fig. 14** (a) Schematic displaying the transition from the rhombohedral to cubic crystal structure in GeTe; (b) DSC plots with the endothermic peaks of pristine GeTe and its derivatives showcasing that with the addition of dopants at the cationic and anionic sites the phase transition temperature ( $T_c$ ) shifts towards lower temperature; (c) plot of phase transition temperature vs.  $\Delta S$ , depicting the shift towards low  $T_c$ . For comparison, Ge<sub>1-x-y</sub>Sb<sub>x</sub>Mn<sub>y</sub>Te was plotted. Reproduced from ref. 144 with permission from the Royal Society of Chemistry.



introduction of imperfections. Thus, chemistry essentially benefits the GeTe thermoelectrics as multiple elements are added simultaneously. The result is that the presence of multiple elements enhances the chemical space, increases the configurational entropy and ultimately provides benefit towards high thermoelectric performance.

**3.3.1.  $(\text{GeTe})_{1-x}(\text{LiSbTe}_2)_x$ .** In Fig. 12, Liu *et al.* alloyed  $\text{LiSbTe}_2$  with GeTe, with an aim to stabilize the cubic structure in the range of 300–773 K. The material provided a superior  $ZT_{\text{avg}}$  of  $\sim 1.38$  in the aforesaid temperature range and can be used for the fabrication of thermoelectric devices.<sup>142</sup> This can be attributed to the fact that in  $\text{LiSbTe}_2$ , the formal charges on Li, Sb and Te are +1, +3 and  $-2$  respectively. This implies that Li has no lone pair, whereas Sb loses the three-5p electrons in the outermost orbital, leaving two electrons in the 5s orbital as the lone pair. However, the  $5s^2$  lone pair on Sb is more stable than the  $4s^2$  lone pair on Ge as the stability of the lone pair increases on descending the group, and so the Sb lone pair is more stable than the Ge lone pair.<sup>143</sup> When alloying with  $\text{LiSbTe}_2$ , where Li and Sb occupy the Ge site partially in both cubic and rhombohedral phases, the average stereochemical activity of the lone pair on the cation is remarkably impeded, causing suppression in the phase-transition temperature. This stabilizes the cubic structure, which promotes the convergence of multiple bands along with phonon scattering. Thus, with the addition of multiple elements the phase transition was averted and the conversion efficiency was raised to 17%, being

one of the highest values among those of polycrystalline p-type alloys.

**3.3.2.  $\text{Ge}_{1-w-x-y}\text{In}_w\text{Pb}_x\text{Sb}_y\text{Te}_{1-z}\text{I}_z$ .** In harmony with the beneficial effect of entropy engineering to suppress the phase transition in GeTe, Qui *et al.* consecutively added multiple dopants continuously. Thermodynamically, the configurational entropy ( $\Delta S$ ) was calculated for multiple species using the equation  $\Delta S = -N_A k_B \sum_{i=1}^n x_i \ln(x_i)$  and is plotted as shown in

Fig. 13(a). The addition of the species shows the increase in the  $\Delta S$  value as  $x$  increases. The powder XRD pattern confirms the formation of more symmetrical crystal structures with the increased number of elements followed by the analysis (Fig. 13(b)), which reveals increase in the lattice parameter along the  $a$ -axis due to the larger atoms at the Ge site as well as the opening of the interaxial angle (Fig. 13(c)).

Moreover, he demonstrated that the addition of the dopants increases the symmetry and brings down the phase transition temperature through DSC measurement as shown in Fig. 14(a)–(c).<sup>144</sup>

Measurement of transport properties (Fig. 15(a)–(c)) validates the finding that an increase in the number of elements increases the Seebeck coefficient, as the entropy engineering promotes band convergence leading to high effective mass, which eventually increases the power factor. Apart from the obvious enhancement in the electronic transport behaviour, the thermal transport properties also show improved behaviour

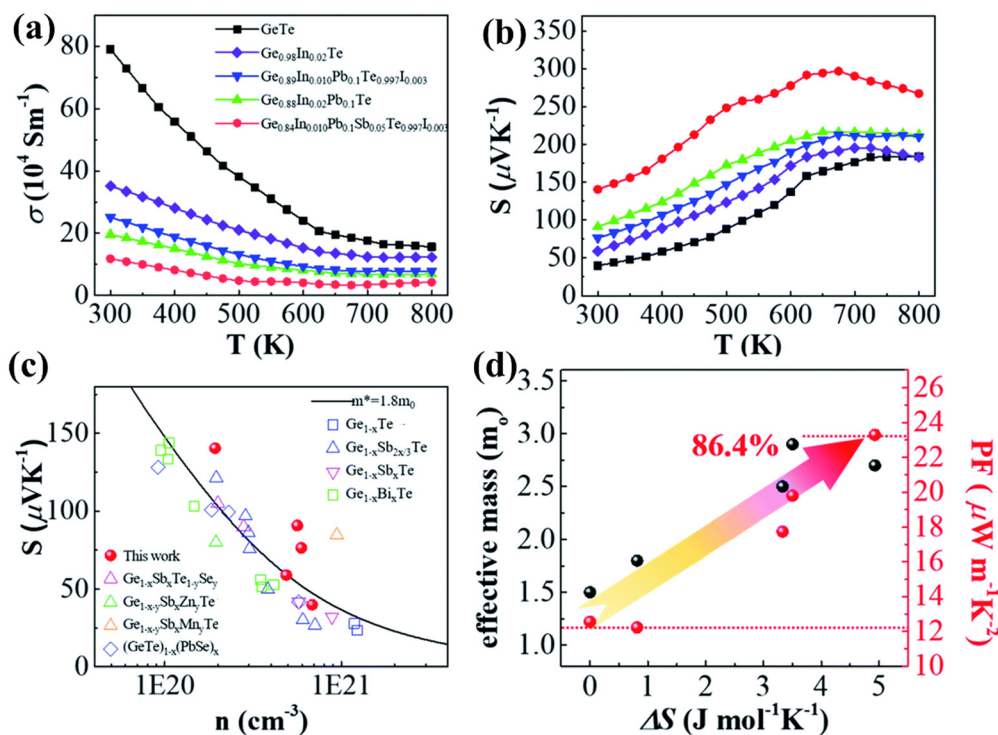


**Fig. 15** Electronic transport properties of pristine GeTe and its derivatives vs. temperature: (a) electrical conductivity; (b) Seebeck coefficient; (c) Pisaranko plot for the Seebeck coefficient with respect to the carrier concentration and (d) change in effective mass and power factor with the increase in the configurational entropy. The plot shows the effect of entropy engineering towards high thermoelectric performance. Data from several other groups were also plotted for comparison. Reproduced from ref. 144 with permission from the Royal Society of Chemistry.



owing to the fact that increase in the dopant introduces point defects (short range disorder) along with long range ordering. Thus, the sites for the scattering of phonons increase leading to diminished lattice thermal conductivity.

Fig. 16(a)–(d) show that the superior entropy alloy is  $\text{Ge}_{0.84}\text{In}_{0.01}\text{Pb}_{0.1}\text{Sb}_{0.05}\text{Te}_{0.997}\text{I}_{0.003}$  with a  $ZT_{\text{peak}}$  of  $\sim 2.1$  at 800 K. If the ferroelectric phase transition can be pulled down at 300 K appropriately, then GeTe based alloys can be efficiently used as power generators for harvesting low-grade heat. Thus, attempts to research novel methods to augment transportation of electrons with damping propagation of phonons if probable, in chorus, will be able to raise the thermoelectric performance.<sup>144</sup>

**3.3.3.  $\text{Ge}_{1-2x-y}\text{Pb}_x\text{Sn}_x\text{Sb}_y\text{Te}$ .** Recently, Das *et al.* in his study mentioned that doping GeTe with 2.5 mol% Pb and Sn each ( $\text{Ge}_{0.95}\text{Pb}_{0.025}\text{Sn}_{0.025}\text{Te}$ ) enriches the configurational entropy in contrast to the pseudoternary systems such as  $\text{PbTe}_{1-2x}\text{Se}_x\text{S}_x$ ,  $\text{SnTe}_{1-2x}\text{Se}_x\text{S}_x$  and  $\text{GeTe}_{1-2x}\text{Se}_x\text{S}_x$ .<sup>145</sup> This is because in the case of pseudo-ternary systems, enthalpy surpasses the entropy and eventually phase separation occurs. The borderline, which separates the secondary phases from the main matrix, scatters the majority charge carriers and the phonons of similar dimensions and hence manifests a negative impact on the thermoelectric properties. However, in 11 mol% Sb-doped  $\text{Ge}_{1-2x}\text{Pb}_x\text{Sn}_x\text{Te}$ , addition of multiple elements

enhances the entropy propelled structural stability in conjunction with an increase in solid solubility limits and hence, the methodology diminishes the phonon conduction ( $\kappa_L$ ) from  $2.8 \text{ W m}^{-1} \text{ K}^{-1}$  for pristine GeTe to  $1.9 \text{ W m}^{-1} \text{ K}^{-1}$  for  $\text{Ge}_{0.95}\text{Pb}_{0.025}\text{Sn}_{0.025}\text{Te}$  samples. The addition of Sb optimizes the carrier concentration by quenching it along with enhancement of the Seebeck coefficient by converging the valence band. Consequently, the ball-milled followed by spark plasma sintered  $\text{Ge}_{0.84}\text{Pb}_{0.025}\text{Sn}_{0.025}\text{Sb}_{0.11}\text{Te}$  displays a much reduced  $\kappa_L$  of  $\sim 1.1 \text{ W m}^{-1} \text{ K}^{-1}$  and a  $ZT_{\text{peak}}$  of 2.3 at 723 K with a  $ZT_{\text{avg}}$  of 1.3 in the 300–723 K range. Provoked by the raised  $ZT$ , a two-leg device was demonstrated with  $\text{Ge}_{0.84}\text{Pb}_{0.025}\text{Sn}_{0.025}\text{Sb}_{0.11}\text{Te}$  (p-type) and I and In doped PbTe (n-type) legs, which exhibits a high output power density of  $\sim 590 \text{ mW cm}^{-2}$  at  $\Delta T = 448 \text{ K}$  as shown in Fig. 17(a)–(d).<sup>85</sup>

**3.3.4.  $\text{Ge}_{1-w-x-y-z}\text{Ag}_w\text{Sb}_x\text{Pb}_y\text{Bi}_z\text{Te}$ .** In a similar experiment conducted by Jiang *et al.*, multiple elements *viz.* Ag, Sb and Pb were alloyed with GeTe due to their enhanced solubility limits.<sup>135</sup> The study reveals the presence of an impurity phase by X-ray diffraction analysis (Fig. 18(a)), when the number of components is three. However, the secondary phase disappears for the alloy with five components due to entropy driven structural stabilization. The single phase was further stabilized by the presence of Cd, Mn and Sn. Transport property measurement shows strong scattering of phonons due to alloying along

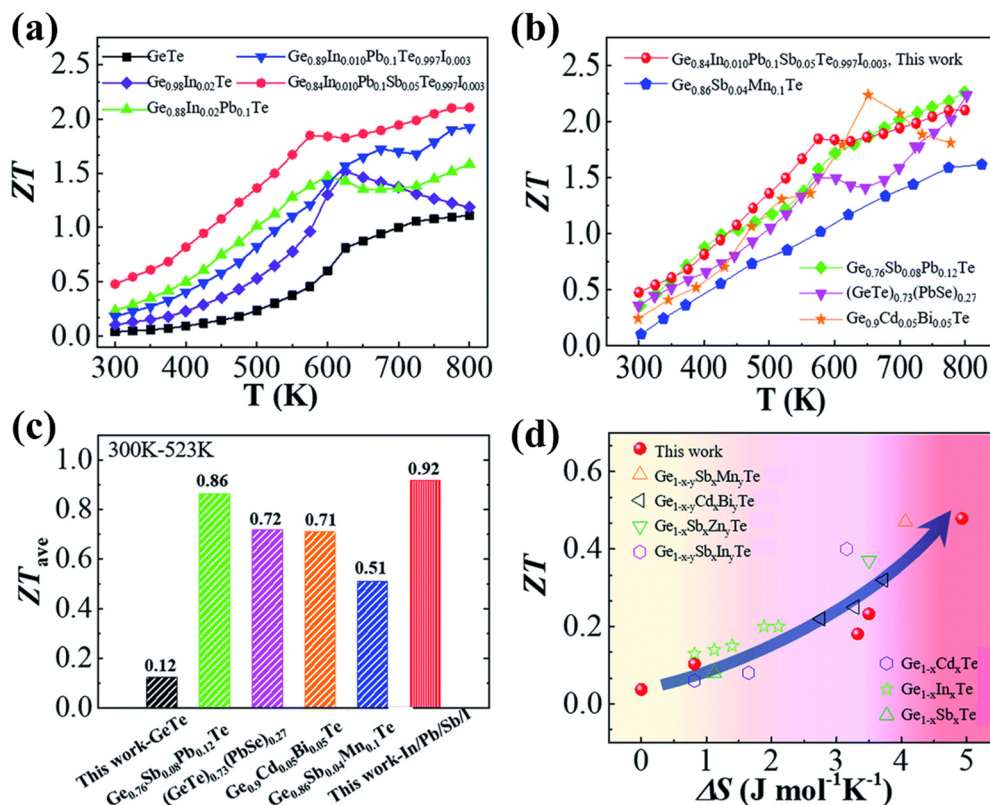


Fig. 16 (a)  $ZT$  values vs.  $T$  for both pristine and GeTe based alloys studied by Qiu *et al.*; (b) highest  $ZT$  values as a function of  $T$  for the high entropy sample studied by Qiu *et al.* and other groups; (c)  $ZT_{\text{ave}}$  of the GeTe samples and GeTe based alloys studied by Qiu *et al.* and other groups in the temperature regime of 300–523 K; (d) variation of  $ZT$  vs. configurational entropy. Reproduced from ref. 144 with permission from the Royal Society of Chemistry.





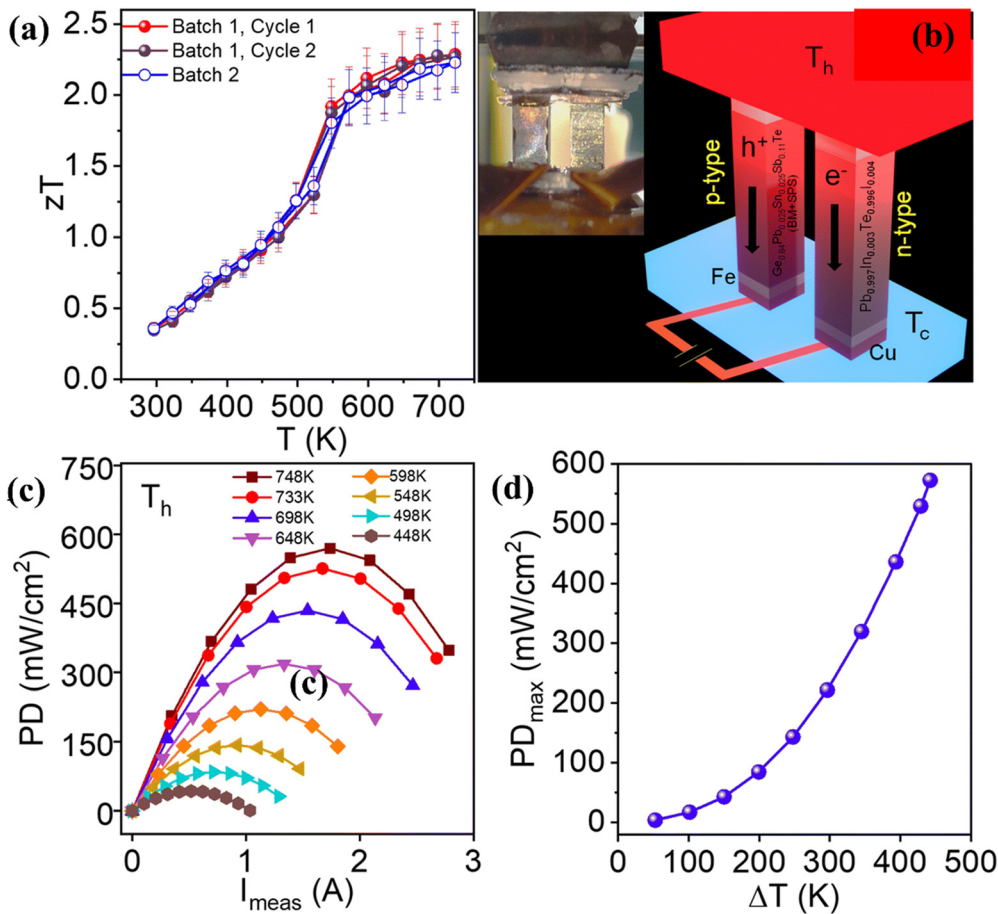


Fig. 17 (a)  $ZT$  of ball-milled followed by spark plasma sintered high entropy GeTe based  $\text{Ge}_{0.84}\text{Pb}_{0.025}\text{Sn}_{0.025}\text{Sb}_{0.11}\text{Te}$  vs.  $T$ . The plot depicts no hysteresis upon thermal cycling. Besides, the data are highly reproducible; (b) demonstration of a two leg thermoelectric module with the  $\text{Ge}_{0.84}\text{Pb}_{0.025}\text{Sn}_{0.025}\text{Sb}_{0.11}\text{Te}$  (p-type) leg and the  $\text{Pb}_{0.997}\text{In}_{0.003}\text{Te}_{0.996}\text{O}_{0.004}$  (n-type) leg. Inset displays the actual image of the device; (c) output power density vs. measured current at different  $\Delta T$ ; and (d) maximum output power density vs.  $\Delta T$  for a two-leg device. Reproduced and adapted from ref. 145.

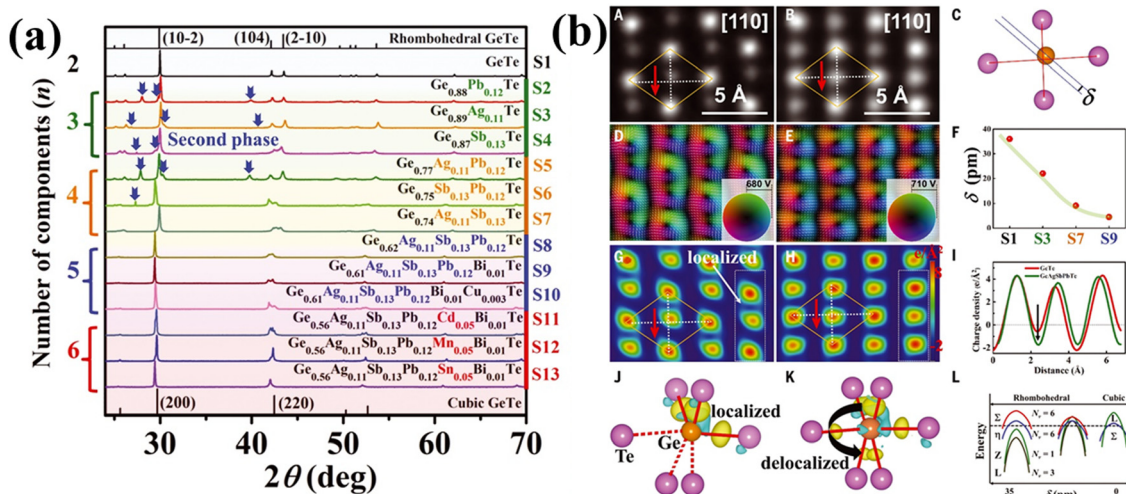


Fig. 18 (a) XRD patterns of GeTe based high entropy materials at room temperature. Secondary phases as indicated by the blue arrow were seen for samples with less components; (b) (A)–(L) images depict the delocalization of the electrons and off-centering of Ge in the high entropy GeTe alloys. Reproduced and adapted from ref. 135. Copyright © 2022, The American Association for the Advancement of Science.



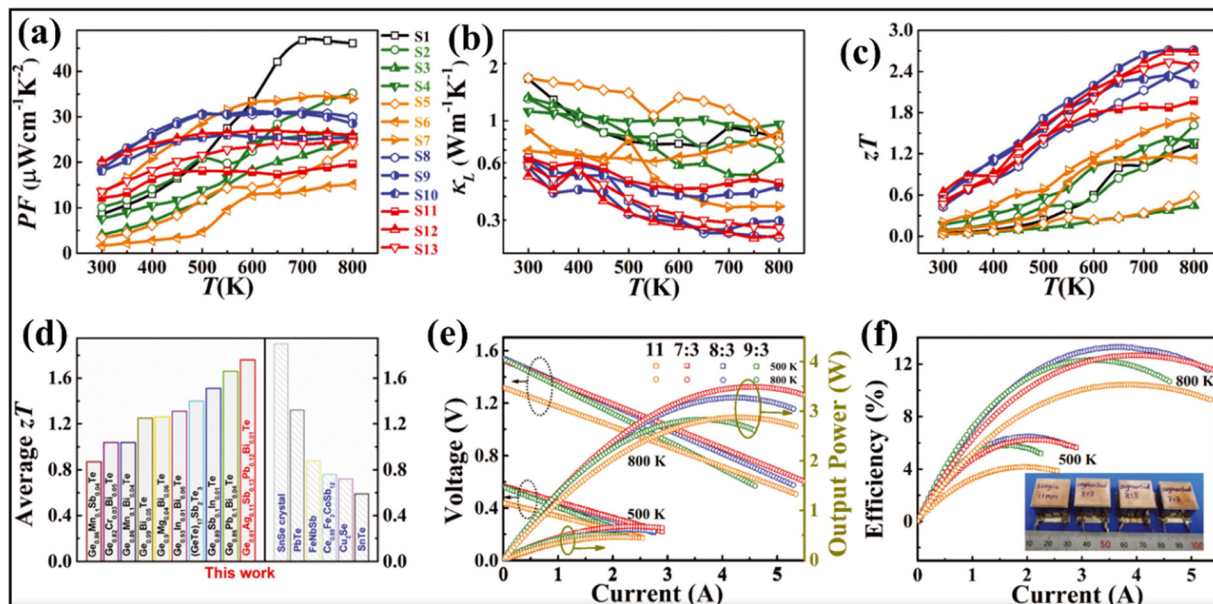


Fig. 19 (a) Power factor; (b) lattice thermal conductivity; (c)  $zT$  vs.  $T$  of the GeTe based alloys studied by Jiang *et al.*; (d) plot to compare the  $ZT_{avg}$  of the GeTe alloys studied by Jiang *et al.* and by other groups and also to compare some of the high  $ZT$  materials, viz. SnSe crystals, PbTe, half-Heusler (FeNbSb), skutterudite ( $Ce_{0.85}Fe_3CoSb_{12}$ ), ionic liquid ( $Cu_2Se$ ) and SnTe; (e) output voltage and output power vs.  $T$ ; and (f) maximum conversion efficiencies vs.  $I$  for the engineered 11, 7 : 3, 8 : 3 and 9 : 3 devices. Reproduced and adapted from ref. 135. Copyright © 2022, The American Association for the Advancement of Science.

with Anderson localization,<sup>146–149</sup> which is actually inevitable in disordered systems and is deleterious for electrons. However, Jiang *et al.*, in his experiment, maintained the Te sublattice

ordered by not adding any constituents at the Te site.<sup>135</sup> Addition of multiple elements at the Ge site causes disorder and eventually Anderson localization. Nevertheless, since the

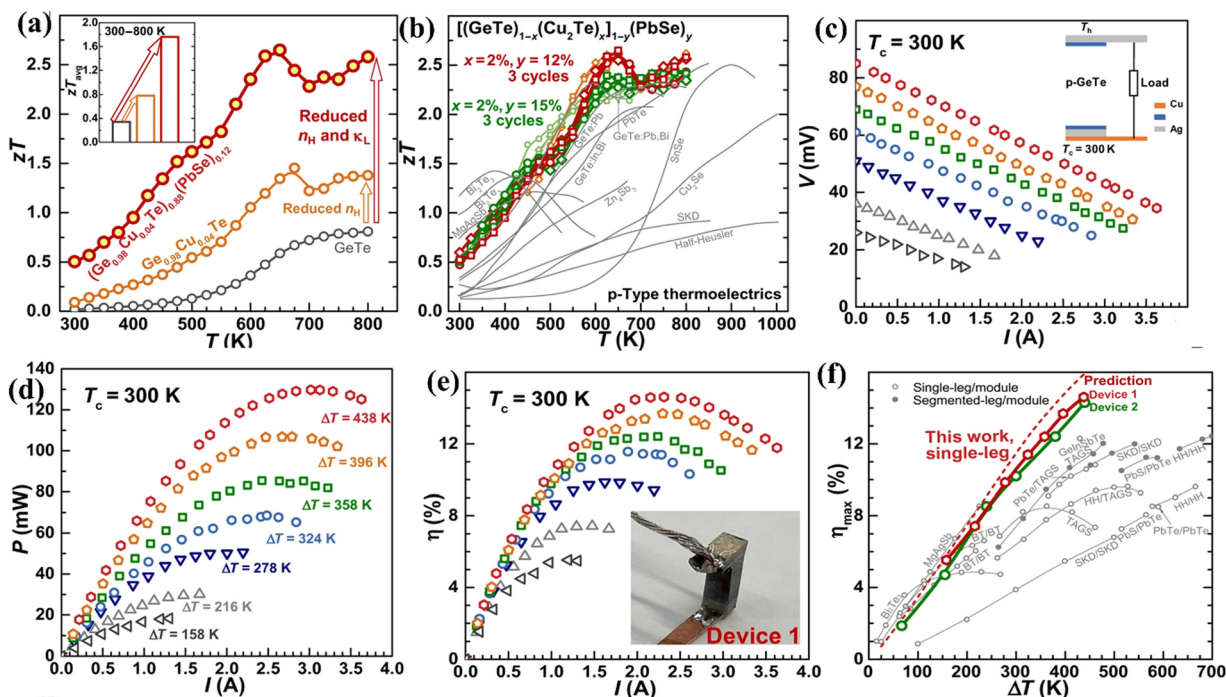


Fig. 20 (a) Change in  $ZT$  and  $ZT_{avg}$  vs.  $T$ ; (b) repeated data acquisition of the high entropy GeTe  $[(Ge_{0.98}Cu_{0.04}Te)_{1-y}(PbSe)_y]$  alloys studied by Bu *et al.* to validate the reproducibility and their comparison with the other reported high-performance p-type thermoelectric alloys; (c) module characteristics; (d) power output; (e) efficiency as a function of current; and (f) maximum efficiency that can be attained for a single leg entropically enriched GeTe alloy as a function of  $\Delta T$  and its comparison with the reported values of TAGS, half-Heusler, and skutterudites and prediction. Reproduced and adapted from ref. 152. Copyright © 2021 under a Creative Commons Attribution Non-Commercial License 4.0 (CC BY-NC).

valence band has more contribution from the 5p orbitals of Te, the impact due to the disordered Ge site on the electron transport properties of p-type GeTe is less. To corroborate the diminished influence of multiple elements in entropy engineered GeTe, the atomic structure was studied for both pristine GeTe and high entropy GeTe based alloys using high-angle annular dark field (HAADF) imaging (*Z*-contrast nature) in the STEM mode. The study reveals more intense spots for high entropy alloys in comparison to the pristine GeTe. Moreover, the Ge atom deviates from the geometric centre of the rhombus created by Te atoms in the GeTe alloy, causing a polarized electric field, the basis of ferroelectricity. The parameter,  $\delta$ , in Fig. 18(b)(C and F) defines the deviation of the Ge atom from the geometric centre. The calculations of atomic resolution HAADF images of GeTe based samples reveal that the  $\delta$  value reduces with the rise in the elemental species and is in concurrence with the XRD results. This indicates the gradual shift from the less symmetric rhombohedral structure to the high symmetry cubic crystal structure for the high entropy alloy and subsequently the faded ferroelectricity.<sup>150,151</sup> This eventually leads to redistribution and delocalization of the electrons. Moreover, all the Ge–Te bond lengths were dissimilar: three shorter bonds due to electron localization and three longer bonds. On the contrary, for the high entropy alloys

wherein there are more alloying elements, the localized electrons undergo transfer of electrons from the shorter to the longer bonds and thus aid in delocalization of electrons. The delocalized electrons thus reduce the energy-offset values amid valence bands and illustrate the raised equivalent degenerated valleys. This ultimately explains the high power factors of entropy-engineered GeTe alloys.

Transport property measurement of the series of samples reveals that electronic conduction is compromised in alloys with multiple elements, while the Seebeck coefficient follows the reverse trend. Consequently, the power factor seems to be low in the low temperature range for the low-entropy alloys *via* scattering of the charge carriers by the multiple phases. The power factor was also low for pure GeTe in the low temperature range owing to the low Seebeck coefficient (Fig. 19(a)). Lattice thermal conductivity (Fig. 19(b)), as expected, shows an ultra-low value in the entire temperature regime, signifying temperature independent behaviour. With all the optimized values, the *ZT* value of  $\text{Ge}_{0.61}\text{Ag}_{0.11}\text{Sb}_{0.13}\text{Pb}_{0.12}\text{Bi}_{0.01}\text{Te}$  was calculated to be 0.6 at 300 K and 2.7 at 750 K (Fig. 19(c)). Thus, the entropy enhancement by multiple element alloying, in contrast to strong alloy scattering and Anderson localisation of the charge carriers, boosts the delocalisation of electrons resulting in improved electrical properties and band convergence. In

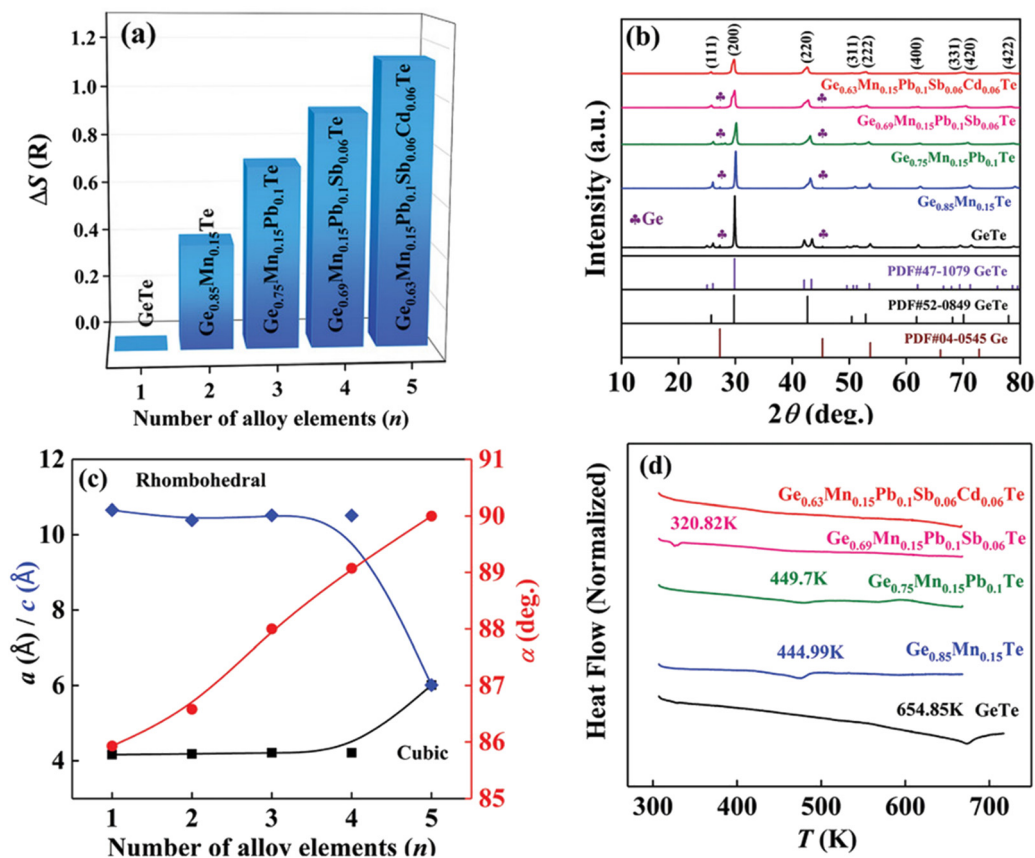


Fig. 21 (a) Configurational entropy  $\Delta S$ , (b) powder XRD patterns, (c) lattice parameter  $a/c$  and interaxial angle,  $\alpha$ , at 300 K, of GeTe-based alloys, and (d) DSC curves showing the lowering of the phase transition temperature of medium entropy GeTe-based alloys. Reproduced and adapted from ref. 154 © 2021 The Authors. Advanced Science published by Wiley-VCH GmbH under the terms of the Creative Commons CC BY license.





addition, the high entropy system dampens the conduction of phonons and thus reduces lattice thermal conductivity. Because of the high  $ZT$  values of the high entropy GeTe alloy, along with average  $ZT$  values higher than those of usual p-type thermoelectric alloys, the thermoelectric module was realized with high experimental conversion efficiency. The module developed using n-type  $\text{Pb}_{0.997}\text{In}_{0.003}\text{Te}_{0.996}\text{I}_{0.004}$  and p-type  $\text{Ge}_{0.61}\text{Ag}_{0.11}\text{Sb}_{0.13}\text{Pb}_{0.12}\text{Bi}_{0.01}\text{Te}$  with a leg length of 11 mm demonstrates a conversion efficiency of 10.5%. However, efforts

were also made to demonstrate the segmented module with low temperature legs using commercially available p-type  $\text{Bi}_{0.5}\text{Sb}_{1.5}\text{Te}_3$  and  $\text{Bi}_2\text{Te}_{2.7}\text{Se}_{0.3}$  as n-type with different (7:3, 8:3 and 9:3) ratios. The 8:3 segmented module displays a significantly high conversion ratio of 13.3% at  $\Delta T = 506$  K. The high conversion efficiency is attributed to the fact of having optimized  $ZT$  in the entire range of operation (Fig. 19(e) and (f)).

3.3.5.  $[(\text{GeTe})_{1-x}(\text{Cu}_2\text{Te})_x]_{1-y}(\text{PbSe})_y$ . In a different experiment conducted by Bu *et al.*, the single leg thermoelectric



Fig. 22 (a) Change in the energy offset value,  $\Delta E$ , with the increase in the alloy elements of four valence bands in GeTe-based alloys; (b) electrical conductivity, (c) Seebeck coefficient, and (f) power factor vs.  $T$  of GeTe-based alloys.<sup>11,54</sup> (d) Variation of  $\alpha$  vs.  $\Delta S$  for pristine GeTe alloys in both rhombohedral and cubic crystal structures as well as for medium and high entropy GeTe-based alloys and their comparison with literature data. (e) Pisarenko plot  $\alpha$  vs.  $n_H$  for medium entropy GeTe-based alloys and their comparison with the literature data. Reproduced and adapted from ref. 154 © 2021 The Authors. Advanced Science published by Wiley-VCH GmbH under the terms of the Creative Commons CC BY license.



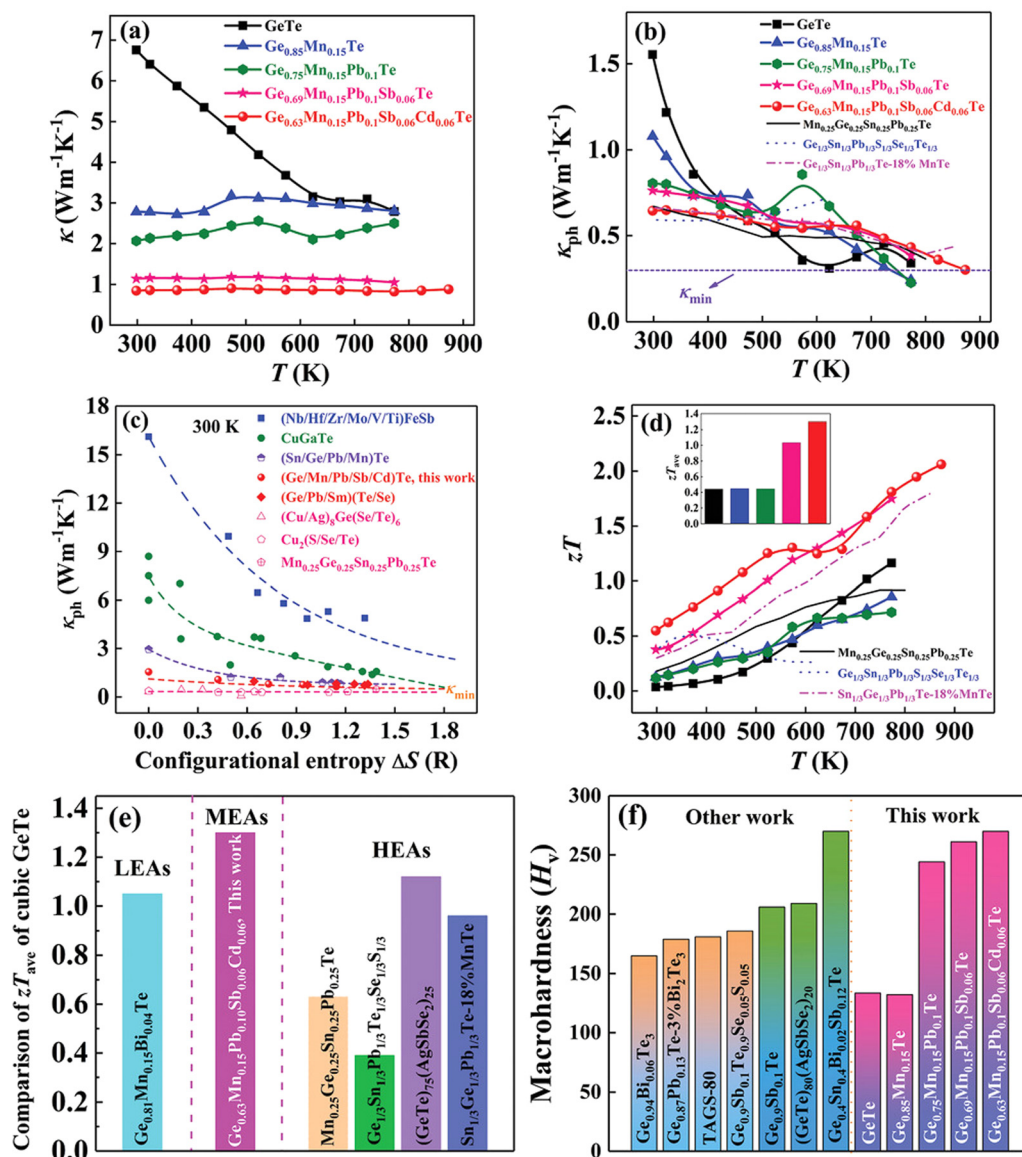


Fig. 23 (a) Total thermal conductivity, (b) lattice thermal conductivity, and (d)  $zT$  vs.  $T$  for medium entropy GeTe-based alloys. Inset (d) displays the  $zT_{\text{avg}}$  values in the operating temperature regime; (c) lattice thermal conductivity vs.  $\Delta S$  for GeTe-based alloys in comparison with literature data. The dashed lines are guides to the eyes. (e) Comparison of  $zT_{\text{avg}}$  of cubic GeTe with different compositions.<sup>11,40,41,44,54</sup> (f) Vickers hardness  $H_V$  of GeTe-based alloys at 300 K compared with literature data. Reproduced and adapted from ref. 154 © 2021 The Authors. Advanced Science published by Wiley-VCH GmbH under the terms of the Creative Commons CC BY license.

Table 1 Configurational entropies of the samples reviewed in this article

Compound	Configurational entropy ( $\Delta S$ ) in $\text{J mol}^{-1} \text{K}^{-1}$
GeTe	5.76
$(\text{GeTe})_{0.7}(\text{LiSbTe}_2)_{0.3}$	9.946
$\text{Ge}_{0.84}\text{In}_{0.01}\text{Pb}_{0.1}\text{Sb}_{0.05}\text{Te}_{0.997}\text{I}_{0.03}$	8.672
$\text{Ge}_{0.84}\text{Pb}_{0.025}\text{Sn}_{0.025}\text{Sb}_{0.11}\text{Te}$	8.144
$\text{Ge}_{0.61}\text{Ag}_{0.11}\text{Sb}_{0.13}\text{Pb}_{0.12}\text{Bi}_{0.01}\text{Te}$	11.169
$(\text{Ge}_{0.98}\text{Cu}_{0.04}\text{Te})_{0.88}(\text{PbSe})_{0.12}$	9.416
$\text{Ge}_{0.63}\text{Mn}_{0.15}\text{Pb}_{0.1}\text{Sb}_{0.06}\text{Cd}_{0.06}\text{Te}$	10.513

device constructed using high entropy GeTe-Cu<sub>2</sub>Te-PbSe  $((\text{Ge}_{1-x}\text{Cu}_x\text{Te})_{1-y}(\text{PbSe})_y)$  alloys displays a conversion

efficiency of 14% at  $\Delta T = 440$  K. The enhanced performance of the alloy was attributed to the optimization of the simultaneous electronic and thermal properties in terms of charge carrier concentration and intensified phonon scattering respectively. Initially, the methodologies adapted to quench the excess carrier concentration had an adverse effect on the carrier mobility. Nonetheless, alloying 1.5%Cu<sub>2</sub>Te was found to be beneficial, as it seemed to reduce hole concentration by one order of magnitude *i.e.*  $\sim 10^{21} \text{ cm}^{-3}$  to  $10^{20} \text{ cm}^{-3}$  without deteriorating the mobility. Moreover, alloying of PbSe suppresses the lattice thermal conductivity along with suppression of formation of Ge vacancies. Within the temperature of operation, the alloy displays a peak  $zT$  of  $> 2.5$  and a  $zT_{\text{avg}}$





Fig. 24 (a) Average energy and average phase transition temperature above the convex hull ( $E_{\text{hull}}$ ) and for alloy compositions respectively that lack one of the constituent elements; (b) and (c) phase-transition temperature vs. work functions of cation and anion compositions. Reproduced with permission from ref. 159 Copyright 2020, American Chemical Society.

of 1.8 and the characteristics of the material and the device are depicted in (Fig. 20(a) and (b)).<sup>152</sup> The output characteristics of the device are shown in (Fig. 20(c)–(e)). The remarkable conversion efficiency of the GeTe based alloy is compared with the reported values of TAGS, half-Heusler, and skutterudites as depicted in Fig. 20(f).

**3.3.6.  $\text{Ge}_{1-w-x-y-z}\text{Mn}_w\text{Pb}_x\text{Sb}_y\text{Cd}_z\text{Te}$ .** Although in the genome of functional materials, configurational entropy is a blooming descriptor,<sup>153</sup> Zhi *et al.* in his study (Fig. 21) explicitly mentioned that due to the adverse effect on carrier mobility in high-entropy alloying, where the principal elements are present with the atomic percentage ranging from 5–35% to accomplish  $\Delta S > 1.5R$ , there is a setback. Instead, he mentioned that medium entropy alloys,  $1R < \Delta S < 1.5R$ , are beneficial as they are capable of balancing the lattice thermal conductivity to attain a glass-like limit in addition to stabilizing the high symmetry cubic crystal structure near room temperature.<sup>154</sup> According to Zhi *et al.*, it is the judicious selection of the alloying species based on the previous reports, to consider, that can aid in realizing high  $ZT$ . Most importantly, the prerequisite condition for an alloying species is that it should have high solid solubility,  $> 5 \text{ mol\%}$  in the main matrix, *i.e.* GeTe. Based on the requirement, Mn, Sb, Pb and Cd were shortlisted to be added at the Ge site. These elements have unique properties: Mn and Cd can aid in band convergence of the valence bands and Pb and Sb quench the high hole concentration of GeTe by raising the  $\Delta G$  of the Ge vacancies. These elements were established as sole dopants and as dual dopants in GeTe; however, their participation in co-alloying GeTe to form a medium entropy alloy was not known. In this regard, the atomic percentages of the elements were adjusted in

a way that  $\Delta S$  was increased to 1.14 for  $\text{Ge}_{0.63}\text{Mn}_{0.15}\text{Pb}_{0.1}\text{Sb}_{0.06}\text{Cd}_{0.06}\text{Te}$  (Fig. 21(a)). Based on the X-ray diffraction pattern, the lattice parameter and interaxial angle were calculated with the increase in the number of alloying elements (Fig. 21(b) and (c)). Differential scanning calorimetry analysis was performed to identify the evolution of phase transition temperature with the enhancement of  $\Delta S$  (Fig. 21(d)). Surprisingly, this medium entropy alloy was capable of suppressing the phase transition temperature at 655 K for GeTe to 300 K and the XRD pattern further confirms the cubic GeTe with the increase of  $\Delta S$ .

The result is that the medium entropy alloy composition  $\text{Ge}_{0.63}\text{Mn}_{0.15}\text{Pb}_{0.1}\text{Sb}_{0.06}\text{Cd}_{0.06}\text{Te}$  could enhance the Seebeck coefficient and reduce lattice thermal conductivity simultaneously without compromising the carrier mobility (Fig. 22). The entropy engineered alloy displayed a  $ZT_{\text{peak}}$  of 2.1 (873 K) and  $ZT_{\text{avg}}$  of 1.3 (300 and 873 K). The results were compared with the data reported in the literature for low- and high-entropy GeTe alloys (Fig. 23), and Table 1 shows the configurational entropies of all the samples reviewed in this article.

The hardness measurement by the Vickers hardness method shows that the mechanical properties of the medium entropy alloy samples are significantly enhanced for practical applications.

## 4. Summary and perspectives

As far as thermoelectricity is concerned, it is always challenging to optimize  $ZT$  due to the inherently intertwined parameters and so various strategies were put forward to decouple and adjust the quasi-independent parameters to enhance the  $ZT$  value. In this review, the concept of entropy engineering was





enlightened with its beneficial effect on GeTe thermoelectrics. It is certainly a difficult task to attain a delicate balance among several prevailing mechanisms to reach the sweet spot of high  $ZT$  by simultaneously reducing the lattice thermal conductivity and without compromising much of the electrical conductivity. Thus, innovative physical mechanisms are always required to push thermoelectrics to a new level of performance, which can be competitive enough with other technologies available for energy conversion and suitable for widespread usage as thermoelectric power generators and coolers.<sup>155</sup>

In the mid temperature range, GeTe based alloys are widely studied eco-friendly thermoelectric materials owing to their excellent thermoelectric performance. Unfortunately, these alloys undergo phase transition at  $\sim 700$  K, and real thermoelectric applications have no space for such phase transitions. However, the result is that it has a low symmetry phase (rhombohedral crystal structure) at low temperature and a high symmetry phase (cubic crystal structure) at high temperature. The high symmetry structure is advantageous for thermoelectrics as it gives high band degeneracy, whereas low symmetry is beneficial because of low phonon conduction. Thus, effort should be put into breaking the symmetry in such a way that both effects can be accomplished simultaneously.

The blooming entropy engineering concept thus applies the idea of adding multiple elements in GeTe for alloying, preferably at the concentration of 5–35 at%. In addition, aliovalent doping at the Ge site also optimizes the carrier concentration, which is otherwise a persistent problem in GeTe and hence it was unexplored for a prolonged period. The alloys thus obtained were high entropy alloys with high configurational entropies, no phase segregation, high symmetry, reduced phase transition temperature, improved power factors and low lattice thermal conductivity but at the cost of reduced mobility. In order to avert this, medium entropy was preferred, where the elements for doping should be such that  $1R < \Delta S < 1.5R$  (Table 1). In this scenario, the carrier mobility is not compromised and high  $ZT$  is obtained.<sup>156,157</sup> The systematic investigation of IV–VI chalcogenides with the thermodynamic landscape of (Ge,Sn,Pb)(S,Se,Te) (as shown in Fig. 24) reveals that a Ge-poor composition at the cationic site and S-poor composition at the anionic site are stable with low phase transition temperature and easy to synthesize.<sup>50,158–161</sup>

The novel theories mentioned above should be executed experimentally with new elements at the cationic and the anionic site to enhance the thermoelectric performance of GeTe based alloys with industrial production at the macroscale. This will enable the macro-fabrication process and real thermoelectric power generator applications.

## Conflicts of interest

There are no conflicts to declare.

## Acknowledgements

The authors would like to acknowledge the members of Thin Film Devices Section for constant support.

## Notes and references

- 1 D. M. Rowe, *CRC Handbook of Thermoelectrics*, CRC, Boca Raton, FL, 1st edn, 1995.
- 2 H. J. Goldsmid and A. W. Penn, *Phys. Lett.*, 1968, **27A**, 523.
- 3 A. J. Minnich, M. S. Dresselhaus, Z. F. Ren and G. Chen, *Energy Environ. Sci.*, 2009, **2**, 466.
- 4 J. R. Sootsman, D. Y. Chung and M. G. Kanatzidis, *Angew. Chem., Int. Ed.*, 2009, **48**, 8616–8619.
- 5 S. Zohreh, Z. Stamatis, C. Boris, S. Sally and C. Yuanlong, *Sustainable Energy Technol. Assess.*, 2020, **37**, 100604.
- 6 C. J. Vineis, A. Shakouri, A. Majumdar and M. G. Kanatzidis, *Adv. Mater.*, 2010, **22**, 3970–3980.
- 7 W. Sun, R. Sui, G. Yuan, H. Zheng, Z. Zeng, P. Xie, L. Yuan, Z. Ren, F. Cai and Q. Zhang, *Mater. Today Phys.*, 2021, **18**, 100391.
- 8 X. L. Shi, J. Zou and Z. G. Chen, *Chem. Rev.*, 2020, **120**(15), 7399–7515.
- 9 R. Basu, *ChemNanoMat*, 2023, **9**, e202200551.
- 10 M. Zebajadi and G. Chen, *APL Mater.*, 2016, **4**, 104401.
- 11 E. Altenkirch, *Phys. Zeitschrift*, 1911, **12**, 920–924.
- 12 A. F. Ioffe, *Semiconductor Thermoelements, and Thermoelectric Cooling*, Infosearch, London, 1957.
- 13 G. S. Nolas, G. A. Slack, J. L. Cohn and S. B. Schujman, The next generation of thermoelectric materials, Seventeenth International Conference on Thermoelectrics. Proceedings ICT98 (Cat. No. 98TH8365), Nagoya, Japan, 1998, pp. 294–297, DOI: [10.1109/ICT.1998.740376](https://doi.org/10.1109/ICT.1998.740376).
- 14 L.-D. Zhao, V. P. Dravid and M. G. Kanatzidis, *Energy Environ. Sci.*, 2014, **7**, 251–268.
- 15 S. Mandava, R. Basu, B. Khasimsaheb, S. Bathula, A. Singh and S. Neeleshwar, *Mater. Adv.*, 2021, **2**, 4352–4361.
- 16 S. Ahmad, A. Singh, S. Bhattacharya, M. Navaneethan, R. Basu, R. Bhatt, P. Sarkar, K. N. Meshram, A. K. Debnath, K. P. Muthe and D. K. Aswal, Band Convergence and Phonon Scattering Mediated Improved Thermoelectric Performance of SnTe–PbTe Nanocomposites, *ACS Appl. Energy Mater.*, 2020, **3**, 8882–8891.
- 17 S. Ahmad, A. Singh, S. Bhattacharya, M. Navaneethan, R. Basu, R. Bhatt, P. Sarkar, K. N. Meshram, K. P. Muthe, S. Vitta and D. K. Aswal, *ACS Appl. Energy Mater.*, 2020, **3**, 7113–7120.
- 18 Z. Li, C. Xiao, H. Zhu and Y. Xie, *J. Am. Chem. Soc.*, 2016, **138**, 14810–14819.
- 19 A. D. LaLonde, Y. Pei, H. Wang and G. J. Snyder, *Mater. Today*, 2011, **14**, 526–532.
- 20 K. Biswas, J. He, I. D. Blum, C.-I. Wu, T. P. Hogan, D. N. Seidman, V. P. Dravid and M. G. Kanatzidis, *Nature*, 2012, **489**, 414–418.
- 21 Y. Xiao and L. D. Zhao, *npj Quantum Mater.*, 2018, **3**, 55.
- 22 O. Delaire, J. Ma and K. Marty, *Nat. Mater.*, 2011, **10**, 614–619.
- 23 Y. Pei, A. LaLonde, S. Iwanaga and G. J. Snyder, *Energy Environ. Sci.*, 2011, **4**, 2085–2089.
- 24 K. Biswas, J. He, G. Wang, S.-H. Lo, C. Uher, V. P. Dravid and M. G. Kanatzidis, *Energy Environ. Sci.*, 2011, **4**, 4675.



- 25 H. J. Wu, L. D. Zhao, F. S. Zheng, D. Wu, Y. L. Pei, X. Tong, M. G. Kanatzidis and J. Q. He, *Nat. Commun.*, 2014, **5**, 4515.
- 26 K. Ahn, K. Biswas, J. He, I. Chung, V. Dravid and M. G. Kanatzidis, *Energy Environ. Sci.*, 2013, **6**, 1529–1537.
- 27 Y. Wu, P. Nan, Z. Chen, Z. Zeng, R. Liu, H. Dong, L. Xie, Y. Xiao, Z. Chen, H. Gu, W. Li, Y. Chen, B. Ge and Y. Pei, *Adv. Sci.*, 2020, **7**, 1902628.
- 28 Y. Pei, A. F. May and G. J. Snyder, *Adv. Energy Mater.*, 2011, **1**, 291–296.
- 29 Y. Pei, A. D. LaLonde, H. Wang and G. J. Snyder, *Energy Environ. Sci.*, 2012, **5**, 7963.
- 30 Z. Wang, G. Wang, R. Wang, X. Zhou, Z. Chen, C. Yin, M. Tang, Q. Hu, J. Tang and R. Ang, *ACS Appl. Mater. Interfaces*, 2018, **10**, 22401–22407.
- 31 Y. Pei, X. Shi, A. LaLonde, H. Wang, L. Chen and G. J. Snyder, *Nature*, 2011, **473**, 66–69.
- 32 H. Liu, Z. Chen, C. Yin, B. Zhou, B. Liu and R. Ang, *Appl. Phys. A: Mater. Sci. Process.*, 2019, **125**, 225.
- 33 P. Jood, M. Ohta, M. Kunii, X. Hu, H. Nishiate, A. Yamamoto and M. G. Kanatzidis, *J. Mater. Chem. C*, 2015, **3**, 10401.
- 34 A. D. LaLonde, Y. Pei and G. Jeffrey Snyder, *Energy Environ. Sci.*, 2011, **4**, 2090.
- 35 Q. Zhang, E. K. Chere, Y. Wang, H. S. Kim, R. He, F. Cao, K. Dahal, D. Broido, G. Chen and Z. Ren, *Nano Energy*, 2016, **22**, 572–582.
- 36 D. Wang, Y. Qin, S. Wang, Y. Qiu, D. Ren, Y. Xiao and L.-D. Zhao, *Ann. Phys.*, 2019, 1900421.
- 37 G. Tan, C. C. Stoumpos, S. Wang, T. P. Bailey, L.-D. Zhao, C. Uher and M. G. Kanatzidis, *Adv. Energy Mater.*, 2017, **7**, 1700099.
- 38 J. Zhang, D. Wu, D. He, D. Feng, M. Yin, X. Qin and J. He, *Adv. Mater.*, 2017, **29**, 1703148.
- 39 K. Ahn, M.-K. Han, J. He, J. Androulakis, S. Ballikaya, C. Uher, V. P. Dravid and M. G. Kanatzidis, *J. Am. Chem. Soc.*, 2010, **132**, 5227–5235.
- 40 K. F. Hsu, S. Loo and F. Guo, *Science*, 2004, **303**, 818–821.
- 41 Y. Zhong, J. Tang, H. Liu, Z. Chen, L. Lin, D. Ren, B. Liu and R. Ang, *ACS Appl. Mater. Interfaces*, 2020, **12**, 49323–49334.
- 42 J. Androulakis, C.-H. Lin, H.-J. Kong, C. Uher, C.-I. Wu, T. Hogan, B. A. Cook, T. Caillat, K. M. Paraskevopoulos and M. G. Kanatzidis, *J. Am. Chem. Soc.*, 2007, **129**, 9780.
- 43 M. H. Lee, J. H. Yun, G. Kim, J. E. Lee, S.-D. Park, H. Reith, G. Schierning, K. Nielsch, W. Ko, A.-P. Li and J.-S. Rhyee, *ACS Nano*, 2019, **13**, 3806–3815.
- 44 Y. Pei, N. A. Heinz, A. LaLonde and G. J. Snyder, *Energy Environ. Sci.*, 2011, **4**, 3640–3645.
- 45 W.-D. Liu, D.-Z. Wang, Q. Liu, W. Zhou, Z. Shao and Z.-G. Chen, *Adv. Energy Mater.*, 2020, **10**, 2000367.
- 46 J. Li, X. Zhang, X. Wang, Z. Bu, L. Zheng, B. Zhou, F. Xiong, Y. Chen and Y. Pei, *J. Am. Chem. Soc.*, 2018, **140**, 16190–16197.
- 47 X. Zhang, Z. Bu, S. Lin, Z. Chen, W. Li and Y. Pei, *Joule*, 2020, **4**, 986–1003.
- 48 S. Perumal, S. Roychowdhury and K. Biswas, *J. Mater. Chem. C*, 2016, **4**, 7520–7536.
- 49 E. Hazan, N. Madar, M. Parag, V. Casian, O. Ben-Yehuda and Y. Gelbstein, Effective Electronic Mechanisms for Optimizing the Thermoelectric Properties of GeTe-Rich Alloys, *Adv. Electron. Mater.*, 2015, **1**, 1500228.
- 50 M. Hong, M. Li, Y. Wang, X.-L. Shi and Z.-G. Chen, *Adv. Mater.*, 2023, **35**, 2208272.
- 51 M. Hong, J. Zou and Z.-G. Chen, Thermoelectric GeTe with Diverse Degrees of Freedom Having Secured Superhigh Performance, *Adv. Mater.*, 2019, **31**, 1807071.
- 52 T. Chatterji, C. M. N. Kumar and U. D. Wdowik, *Phys. Rev. B*, 2015, **91**, 054110.
- 53 U. V. Waghmare, N. A. Spaldin, H. C. Kandpal and R. Seshadri, *Phys. Rev. B*, 2003, **67**, 125111.
- 54 M. Hong, Z.-G. Chen, L. Yang, Y.-C. Zou, M. S. Dargusch, H. Wang and J. Zou, *Adv. Mater.*, 2018, **30**, 1705942.
- 55 P. Gorai, P. Parilla, E. S. Toberer and V. Stevanović, *Chem. Mater.*, 2015, **27**, 6213–6221.
- 56 J. Li, Z. Chen, X. Zhang, H. Yu, Z. Wu, H. Xie, Y. Chen and Y. Pei, *Adv. Sci.*, 2017, **4**, 1700341.
- 57 X. Wang, W. Xue, Z. Zhang, X. Li, L. Yin, C. Chen, B. Yu, J. Sui, F. Cao, X. Liu, J. Mao, Y. Wang, X. Lin and Q. Zhang, Stabilizing the Optimal Carrier Concentration in Al/Sb-Codoped GeTe for High Thermoelectric Performance, *ACS Appl. Mater. Interfaces*, 2021, **13**, 45717–45725.
- 58 L. Xu, G. Wu, R. Wang, Z. Yan, J. Cai, J. Yang, X. Wang, J. Luo, X. Tan, G. Liu and J. Jiang, *ACS Appl. Mater. Interfaces*, 2022, **14**, 14359–14366.
- 59 A. Suwardi, J. Cao, Y. Zhao, J. Wu, S. W. Chien, X. Y. Tan, L. Hu, X. Wang, W. Wang, D. Li, Y. Yin, W.-X. Zhou, D. V. M. Repaka, J. Chen, Y. Zheng, Q. Yan, G. Zhang and J. Xu, *Mater. Today Phys.*, 2020, **14**, 100239.
- 60 Y. Jin, Y. Xiao, D. Wang, Z. Huang, Y. Qiu and L.-D. Zhao, *ACS Appl. Energy Mater.*, 2019, **2**, 7594–7601.
- 61 J. Dong, J. Gao and Q. Yan, *Mater. Lab.*, 2023, **2**, 230001.
- 62 Y. F. Ye, Q. Wang, J. Lu, C. T. Liu and Y. Yang, *Mater. Today*, 2016, **19**, 349–362.
- 63 E. P. George, D. Raabe and R. O. Ritchie, *Nat. Rev. Mater.*, 2019, **4**, 515–534.
- 64 Y. Zhang, T. T. Zuo, Z. Tang, M. C. Gao, K. A. Dahmen, P. K. Liaw and Z. P. Lu, *Prog. Mater. Sci.*, 2014, **61**, 1–93.
- 65 D. B. Miracle and O. N. Senkov, *Acta Mater.*, 2017, **122**, 448–511.
- 66 J. W. Yeh, S. K. Chen, S. J. Lin, J. Y. Gan, T. S. Chin, T. T. Shun, C. H. Tsau and S. Y. Chang, *Adv. Eng. Mater.*, 2004, **6**, 299–303.
- 67 B. S. Murty, J. W. Yeh and S. Ranganathan, *High-Entropy Alloys*, Butterworth-Heinemann, London, 2014.
- 68 B. Cantor, I. T. H. Chang, P. Knight and A. J. B. Vincent, *Mater. Sci. Eng., A*, 2004, **375–377**, 213.
- 69 X. Chang, M. Zeng, K. Liu and L. Fu, *Adv. Mater.*, 2020, **32**, 1907226.
- 70 D. K. Aswal, R. Basu and A. Singh, *Energy Convers. Manage.*, 2016, **114**, 50–67.



- 71 L. Hu, Y. Zhang, H. Wu, J. Li, Y. Li, M. McKenna, J. He, F. Liu, S. J. Pennycook and X. Zeng, *Adv. Energy Mater.*, 2018, **8**, 1802116.
- 72 M. A. Buckingham, B. Ward-O'Brien, W. Xiao, Y. Li, J. Qu and D. J. Lewis, *Chem. Commun.*, 2022, **58**, 8025–8037.
- 73 R. Z. Zhang, F. Gucci, H. Zhu, K. Chen and M. J. Reece, *Inorg. Chem.*, 2018, **57**, 13027–13033.
- 74 J.-Y. Liu, L. Chen and L.-M. Wu, *Nat. Commun.*, 2022, **13**, 2966.
- 75 R. Chen, P. Qiu, B. Jiang, P. Hu, Y. Zhang, J. Yang, R. X. Shi and L. Chen, *J. Mater. Chem. A*, 2018, **6**, 6493–6502.
- 76 C. R. McCormick and R. E. Schaak, *J. Am. Chem. Soc.*, 2021, **143**, 1017–1023.
- 77 J. Li, X. Zhang, Z. Chen, S. Lin, W. Li, J. Shen, I. T. Witting, A. Faghaninia, Y. Chen, A. Jain, L. Chen, G. J. Snyder and Y. Pei, *Joule*, 2018, **2**, 976–987.
- 78 M. Hong, K. Zheng, W. Lyv, M. Li, X. Qu, Q. Sun, S. Xu, J. Zou and Z.-G. Chen, *Energy Environ. Sci.*, 2020, **13**, 1856–1864.
- 79 M. Hong and Z.-G. Chen, *Acc. Chem. Res.*, 2022, **55**, 3178–3190.
- 80 N. Man, J. Cai, Z. Guo, G. Liu, P. Sun, H. Wang, Q. Zhang, X. Tan, Y. Yin and J. Jiang, *ACS Appl. Energy Mater.*, 2021, **4**, 4242–4247.
- 81 Z. Liu, J. Sun, J. Mao, H. Zhu, W. Ren, J. Zhou, Z. Wang, D. J. Singh, J. Sui, C.-W. Chu and Z. Ren, *Proc. Natl. Acad. Sci. U. S. A.*, 2018, **115**, 5332.
- 82 S. Perumal, M. Samanta, T. Ghosh, U. S. Shenoy, A. K. Bohra, S. Bhattacharya, A. Singh, U. V. Waghmare and K. Biswas, *Joule*, 2019, **3**, 2565–2580.
- 83 Y. Jin, D. Wang, Y. Qiu and L.-D. Zhao, *J. Mater. Chem. C*, 2021, **9**, 6484–6490.
- 84 M. Hong, Y. Wang, T. Feng, Q. Sun, S. Xu, S. Matsumura, S. T. Pantelides, J. Zou and Z.-G. Chen, *J. Am. Chem. Soc.*, 2019, **141**, 1742–1748.
- 85 E. Nshimiyimana, S. Hao, X. Su, C. Zhang, W. Liu, Y. Yan, C. Uher, C. Wolverton, M. G. Kanatzidis and X. Tang, *J. Mater. Chem. A*, 2020, **8**, 1193–1204.
- 86 M. Hong, Y. Wang, W. Liu, S. Matsumura, H. Wang, J. Zou and Z.-G. Chen, *Adv. Energy Mater.*, 2018, **8**, 1801837.
- 87 A. Swardi, J. Cao, L. Hu, F. Wei, J. Wu, Y. Zhao, S. H. Lim, L. Yang, X. Y. Tan, S. W. Chien, Y. Yin, W.-X. Zhou, W. L. M. Nancy, X. Wang, S. H. Lim, X. Ni, D. Li, Q. Yan, Y. Zheng, G. Zhang and J. Xu, *J. Mater. Chem. A*, 2020, **8**, 18880–18890.
- 88 A.-C. Yeh, S. Gorsse, V. Keppens and D. A. Gilbert, *APL Mater.*, 2023, **11**, 030402.
- 89 X. Wang, W. Guo and Y. Fu, *J. Mater. Chem. A*, 2021, **9**, 663–701.
- 90 R. Chen, Y. Yan, W. Zhang, F. Liu, H. Kang, E. Guo, Z. Chen and T. Wang, *Chem. Mater.*, 2023, **35**, 2202–2212.
- 91 Z. Lei, X. Liu, H. Wang, Y. Wu, S. Jiang and Z. Lu, *Scr. Mater.*, 2019, **165**, 164–169.
- 92 Y. Zhang, Y. J. Zhou, J. P. Lin, G. L. Chen and P. K. Liaw, *Adv. Eng. Mater.*, 2008, **10**, 534–538.
- 93 B. Jiang, Y. Yu, H. Chen, J. Cui, X. Liu, L. Xie and J. He, *Nat. Commun.*, 2021, **12**, 3234.
- 94 A. Ruffa, *Phys. Rev. B: Condens. Matter Mater. Phys.*, 1982, **25**, 5895.
- 95 C. A. Gearhart, *Am. J. Phys.*, 1990, **58**, 468–480.
- 96 R. Basu, S. Bhattacharya, R. Bhatt, M. Roy, S. Ahmad, A. Singh, M. Navaneethan, Y. Hayakawa, D. K. Aswal and S. K. Gupta, *J. Mater. Chem. A*, 2014, **2**, 6922–6930.
- 97 R. Basu and A. Singh, *Mater. Today Phys.*, 2021, **21**, 100468.
- 98 S. Ahmad, R. Basu, P. Sarkar, A. Singh, A. Bohra, S. Bhattacharya, R. Bhatt, K. N. Meshram, S. Samanta, P. Bhatt, M. Navaneethan, Y. Hayakawa, A. K. Debnath, S. K. Gupta, D. K. Aswal, K. P. Muthe and S. C. Gadkari, *Materialia*, 2018, **4**, 147–156.
- 99 A. K. Bohra, R. Bhatt, A. Singh, S. Bhattacharya, R. Basu, P. Bhatt, M. Navaneethan, S. K. Sarkar, S. Anwar, K. P. Muthe and D. K. Aswal, *Phys. Status Solidi RRL*, 2020, **14**, 2000102.
- 100 S. Bhattacharya, R. Basu, R. Bhatt, S. Pitale, A. Singh, D. K. Aswal, S. K. Gupta, M. Navaneethan and Y. Hayakawa, *J. Mater. Chem. A*, 2013, **1**, 11289–11294.
- 101 S. Bhattacharya, A. Bohra, R. Basu, R. Bhatt, S. Ahmad, K. N. Meshram, A. K. Debnath, A. Singh, S. K. Sarkar, M. Navaneethan, Y. Hayakawa, D. K. Aswal and S. K. Gupta, *J. Mater. Chem. A*, 2014, **2**, 17122–17129.
- 102 Z. Dong, J. Luo, C. Wang, Y. Jiang, S. Tan, Y. Zhang, Y. Grin, Z. Yu, K. Guo, J. Zhang and W. Zhang, *Nat. Commun.*, 2022, **13**, 35.
- 103 H. Zhu, W. Li, A. Nozariasbmarz, N. Liu, Y. Zhang, S. Priya and B. Poudel, *Nat. Commun.*, 2023, **14**, 3300.
- 104 S. M. Kauzlarich, S. R. Brown and G. J. Snyder, *Dalton Trans.*, 2007, 2099–2107.
- 105 J. Shuai, J. Mao, S. Song, Q. Zhang, G. Chen and Z. Ren, *Mater. Today Phys.*, 2017, **1**, 74–95.
- 106 Y. Xing, R. Liu, J. Liao, C. Wang, Q. Zhang, Q. Song, X. Xia, T. Zhu, S. Bai and L. Chen, *Joule*, 2020, **4**, 2475–2483.
- 107 S. K. Sahu, A. K. Bohra, P. G. Abichandani, A. Singh, S. Bhattacharya, R. Bhatt, R. Basu, P. Sarkar, S. K. Gupta, K. P. Muthe and S. C. Gadkari, Design and development of DC to DC voltage booster to integrate with PbTe/TAGS-85 based thermoelectric power generators, *Mater. Sci. Energy Tech.*, 2019, **2**, 429–433.
- 108 B. Zhu, X. Liu, Q. Wang, Y. Qiu, Z. Shu, Z. Guo, Y. Tong, J. Cui, M. Guo and J. He, *Energy Environ. Sci.*, 2020, **13**, 2106.
- 109 Y. Sun, F. Guo, Y. Feng, C. Li, Y. Zou, J. Cheng, X. Dong, H. Wu, Q. Zhang, W. Liu, Z. Liu, W. Cai, Z. Ren and J. Sui, *Nat. Commun.*, 2023, **14**, 8085.
- 110 Q. Shi, J. Li, X. Zhao, Y. Chen, F. Zhang, Y. Zhong and R. Ang, *ACS Appl. Mater. Interfaces*, 2022, **14**, 49425–49445.
- 111 S. Y. Tee, D. Ponsford, C. L. Lay, X. Wang, X. Wang, D. C. J. Neo, T. Wu, W. Thitsartarn, J. C. C. Yeo, G. Guan, T.-C. Lee and M.-Y. Han, *Adv. Sci.*, 2022, **9**, 2204624.
- 112 H. Wu, X.-L. Shi, J. Duan, Q. Liu and Z.-G. Chen, *Energy Environ. Sci.*, 2023, **16**, 1870–1906.
- 113 S. Huang, T.-R. Wei, H. Chen, J. Xiao, M. Zhu, K. Zhao and X. Shi, *ACS Appl. Mater. Interfaces*, 2021, **13**, 60192–60199.





- 114 N. Jakhar, D. K. Kedia, A. Kumar, K. Saurabh and S. Singh, *Appl. Phys. Lett.*, 2023, **122**, 163901.
- 115 J. Zhang, M. Nisar, H. Xu, F. Li, Z. Zheng, G. Liang, P. Fan and Y.-X. Chen, *ACS Appl. Mater. Interfaces*, 2023, **15**, 47158–47167.
- 116 T.-R. Wei, P. Qiu, K. Zhao, X. Shi and L. Chen, *Adv. Mater.*, 2023, **35**, 2110236.
- 117 J.-Y. Raty, M. Schumacher, P. Golub, V. L. Deringer, C. Gatti and M. Wuttig, *Adv. Mater.*, 2019, **31**, 1806280.
- 118 M. Wuttig, V. L. Deringer, X. Gonze, C. Bichara and J.-Y. Raty, *Adv. Mater.*, 2018, **30**, 1803777.
- 119 Y. Yu, M. Cagnoni, O. Cojocaru-Mirédin and M. Wuttig, *Adv. Funct. Mater.*, 2020, **30**, 1904862.
- 120 I. Maria, R. Arora, M. Dutta, S. Roychowdhury, U. V. Waghmare and K. Biswas, *J. Am. Chem. Soc.*, 2023, **145**, 9292–9303.
- 121 R. Basu, C. Nayak, R. Kumar, D. Bhattacharyya, S. N. Jha and A. Singh, *ACS Appl. Energy Mater.*, 2023, **6**(5), 2981–2988.
- 122 W. Zhang, H. Zhang, S. Sun, X. Wang, Z. Lu, X. Wang, J.-J. Wang, C. Jia, C.-F. Schön, R. Mazzarello, E. Ma and M. Wuttig, *Adv. Sci.*, 2023, **10**, 2300901.
- 123 S. Li, X. Li, Z. Ren and Q. Zhang, *J. Mater. Chem. A*, 2018, **6**, 2432–2448.
- 124 M. Zhou, G. J. Snyder, L. Li and L.-D. Zhao, *Inorg. Chem. Front.*, 2016, **3**, 1449–1463.
- 125 A. Banik, S. Roychowdhury and K. Biswas, *Chem. Commun.*, 2018, **54**, 6573–6590.
- 126 M. K. Brod, M. Y. Toriyama and G. J. Snyder, *Chem. Mater.*, 2020, **32**, 9771–9779.
- 127 S. Roychowdhury, M. Samanta, S. Perumal and K. Biswas, *Chem. Mater.*, 2018, **30**, 5799–5813.
- 128 C. Wang, Z. Zeng, Y. Chen, J. Wu, J. Ma, J. Embs, Y. Pei and Y. Chen, *npj Comput. Mater.*, 2021, **7**, 118.
- 129 M. Li, M. Hong, X. Tang, Q. Sun, W.-Y. Lyu, S.-D. Xu, L.-Z. Kou, M. Dargusch, J. Zou and Z.-G. Chen, *Nano Energy*, 2020, **73**, 104740.
- 130 A. Suwardi, D. Bash, H. K. Ng, J. R. Gomez, D. V. M. Repaka, P. Kumara and K. Hippalgaonkar, *J. Mater. Chem. A*, 2019, **7**, 23762–23769.
- 131 W. Li and M. Liu, *ACS Appl. Electron. Mater.*, 2023, **5**, 4523–4533.
- 132 A. Li, C. Hu, B. He, M. Yao, C. Fu, Y. Wang, X. Zhao, C. Felser and T. Zhu, *Nat. Commun.*, 2021, **12**, 5408.
- 133 N. Wang, M. Li, H. Xiao, Z. Gao, Z. Liu, X. Zu, S. Li and L. Qiao, *npj Comput. Mater.*, 2021, **7**, 18.
- 134 H. Namiki, M. Kobayashi, K. Nagata, Y. Saito, N. Tachibana and Y. Ota, *Mater. Today Sustainable*, 2022, **18**, 100116.
- 135 B. Jiang, W. Wang, S. Liu, Y. Wang, C. Wang, Y. Chen, L. Xie, M. Huang and J. He, *Science*, 2022, **377**, 208–213.
- 136 S. Roychowdhury and K. Biswas, Slight Symmetry Reduction in Thermoelectrics, *Chem*, 2018, **4**, 939–942.
- 137 S. S. Aamlid, M. Oudah, J. Rottler and A. M. Hallas, *J. Am. Chem. Soc.*, 2023, **145**, 5991–6006.
- 138 R. Basu, S. Mandava, U. S. Shenoy, D. K. Bhat, B. Khasimsaheb, A. K. Debnath, A. Singh and S. Neeleshwar, *Mater. Adv.*, 2021, **2**, 7891–7906.
- 139 W.-Y. Ching, S. San, J. Brechtel, R. Sakidja, M. Zhang and P. K. Liaw, *npj Comput. Mater.*, 2020, **6**, 45.
- 140 Y. Jiang, J. Dong, H.-L. Zhuang, J. Yu, B. Su, H. Li, J. Pei, F.-H. Sun, M. Zhou, H. Hu, J.-W. Li, Z. Han, B.-P. Zhang, T. Mori and J.-F. Li, *Nat. Commun.*, 2022, **13**, 6087.
- 141 B. Jiang, Y. Yu, J. Cui, X. Liu, L. Xie, J. Liao, Q. Zhang, Y. Huang, S. Ning, B. Jia, B. Zhu, S. Bai, L. Chen, S. J. Pennycook and J. He, *Science*, 2021, **371**, 830–834.
- 142 M. Liu, J. Zhu, B. Cui, F. Guo, Z. Liu, Y. Zhu, M. Guo, Y. Sun, Q. Zhang, Y. Zhang, W. Cai and J. Sui, *Cell Rep. Phys. Sci.*, 2022, **3**, 100902.
- 143 M. J. Smiles, J. M. Skelton, H. Shiel, L. A. H. Jones, J. E. N. Swallow, H. J. Edwards, P. A. E. Murgatroyd, T. J. Featherstone, P. K. Thakur, T.-L. Lee, V. R. Dhanak and T. D. Veal, *J. Mater. Chem. A*, 2021, **9**, 22440–22452.
- 144 Y. Qiu, Y. Jin, D. Wang, M. Guan, W. He, S. Peng, R. Liu, X. Gao and L.-D. Zhao, *J. Mater. Chem. A*, 2019, **7**, 26393–26401.
- 145 A. Das, P. Acharyya, S. Das and K. Biswas, *J. Mater. Chem. A*, 2023, **11**, 12793–12801.
- 146 Z. Tian, *ACS Nano*, 2019, **13**, 3750–3753.
- 147 S. Roychowdhury, T. Ghosh, R. Arora, M. Samanta, L. Xie, N. K. Singh, A. Soni, J. He, U. V. Waghmare and K. Biswas, *Science*, 2021, **371**, 722–727.
- 148 M. T. Agne, F. R. L. Lange, J. P. Male, K. S. Siegert, H. Volker, C. Poltorak, A. Poitz, T. Siegrist, S. Maier, G. J. Snyder and M. Wuttig, *Matter*, 2021, **4**, 2970–2984.
- 149 K. Yamamoto, A. Aharony, O. Entin-Wohlman and N. Hatano, *Phys. Rev. B*, 2017, **96**, 155201.
- 150 E. M. Levin, M. F. Besser and R. Hanus, *J. Appl. Phys.*, 2013, **114**, 083713.
- 151 D. Di Sante, P. Barone, R. Bertacco and S. Picozzi, *Adv. Mater.*, 2013, **25**, 509–513.
- 152 Z. Bu, X. Zhang, B. Shan, J. Tang, H. Liu, Z. Chen, S. Lin, W. Li and Y. Pei, *Sci. Adv.*, 2021, **7**, 2738.
- 153 R. H. Liu, H. Y. Chen, K. P. Zhao, Y. T. Qin, B. B. Jiang, T. S. Zhang, G. Sha, X. Shi, C. Uher, W. Q. Zhang and L. D. Chen, *Adv. Mater.*, 2017, **29**, 1702712.
- 154 S. Zhi, J. Li, L. Hu, J. Li, N. Li, H. Wu, F. Liu, C. Zhang, W. Ao, H. Xie, X. Zhao, S. J. Pennycook and T. Zhu, *Adv. Sci.*, 2021, **8**, 2100220.
- 155 C. Xu, Z. Liang, W. Ren, S. Song, F. Zhang and Z. Ren, *Adv. Energy Mater.*, 2022, **12**, 2202392.
- 156 M. Zhang, Z. Gao, Q. Lou, Q. Zhu, J. Wang, Z. Han, C. Fu and T. Zhu, *Adv. Funct. Mater.*, 2023, 2307864.
- 157 D.-Z. Wang, W.-D. Liu, M. Li, K. Zheng, H. Hu, L.-C. Yin, Y. Wang, H. Zhu, X.-L. Shi, X. Yang, Q. Liu and Z.-G. Chen, *Adv. Funct. Mater.*, 2023, **33**, 2213040.
- 158 S. Roychowdhury, T. Ghosh, R. Arora, U. V. Waghmare and K. Biswas, *Angew. Chem., Int. Ed.*, 2018, **57**, 15167.
- 159 Z. H. Deng, A. Olvera, J. Casamento, J. S. Lopez, L. Williams, R. Lu, G. S. Shi, P. F. P. Poudeu and E. Kioupakis, *Chem. Mater.*, 2020, **32**, 6070.
- 160 C. X. Zhang, C. Y. Wang, Y. C. Xie, B. Chen and C. H. Zhang, *Mater. Des.*, 2018, **157**, 394.
- 161 J. Tang, Z. Yao, Y. Wu, S. Lin, F. Xiong, W. Li, Y. Chen, T. Zhu and Y. Pei, *Mater. Today Phys.*, 2020, **15**, 100247.

